JGR Oceans

RESEARCH ARTICLE
10.1029/2023JC020010

An ARGO and XBT Observing System for the Atlantic Meridional Overturning Circulation and Meridional Heat Transport (AXMOC) at 22.5°S

I. Pita[1,2,3], M. Goes[2,3], D. L. Volkov[2,3], S. Dong[3], G. Goni[3], and M. Cirano[4]

[1]Rosenstiel School, University of Miami, Miami, FL, USA, [2]Cooperative Institute for Marine and Atmospheric Studies, University of Miami, Miami, FL, USA, [3]Atlantic Oceanographic and Meteorological Laboratory, NOAA, Miami, FL, USA, [4]Department of Meteorology, Institute of Geosciences, Federal University of Rio de Janeiro (UFRJ), Rio de Janeiro, Brazil

Key Points:

- First in situ estimates of the Atlantic Meridional Overturning Circulation and Meridional Heat Transport time series at 22.5°S
- Mapping method developed here captures the coastal sea level and westward propagating features
- Interannual variability of the overturning at 22.5°S is dominated by western boundary currents, followed by eastern boundary currents

Supporting Information:

Supporting Information may be found in the online version of this article.

Correspondence to:

I. Pita,
ivenis.pita@noaa.gov

Citation:

Pita, I., Goes, M., Volkov, D. L., Dong, S., Goni, G., & Cirano, M. (2024). An ARGO and XBT observing system for the Atlantic Meridional Overturning Circulation and Meridional Heat Transport (AXMOC) at 22.5°S. *Journal of Geophysical Research: Oceans*, *129*, e2023JC020010. https://doi.org/10.1029/2023JC020010

Received 7 MAY 2023
Accepted 5 DEC 2023

Abstract Changes in the Atlantic Meridional Overturning Circulation (AMOC) and associated Meridional Heat Transport (MHT) can affect climate and weather patterns, regional sea levels, and ecosystems. Direct observations of the AMOC are still limited, particularly in the South Atlantic. This study establishes a cost-effective trans-basin section to estimate for the first time the AMOC and MHT at 22.5°S, using only sustained ocean observations. For this, an optimal mapping method that minimizes the difference between surface in situ dynamic height and satellite altimetry was developed to retrieve monthly temperature and salinity profiles from Argo and XBT data along the 22.5°S section. The mean states, as well as the interannual and seasonal changes of the obtained AMOC and MHT were compared with other products. The mean AMOC and MHT for 22.5°S are 16.3 ± 3.2 Sv and 0.7 ± 0.2 PW, respectively, showing stronger transports during austral fall/winter and weaker in spring. The high-density XBT data available at the western boundary were vital for capturing the highly variable Brazil Current (BC), whose mean and variability was improved compared to other products. At 22.5°S, the North Atlantic Deep Water is divided into two cores that flow along both the western and the eastern boundaries near 2,500 m depth. Our results (a) suggest a greater influence of the western boundary current system on the AMOC variability at 22.5°S, (b) highlight the importance of high-density in situ data for AMOC estimates, and (c) contribute to a better understanding of the AMOC and MHT variability in the South Atlantic.

Plain Language Summary The Atlantic Meridional Overturning Circulation (AMOC) is a system of ocean currents responsible for the north-south movement of water, heat, and other properties, which influences climate, weather, sea level, and ecosystems. Because direct measurements of this circulation are limited in space and time, especially in the South Atlantic, most observational estimates of the overturn here are based on statistical relationships between satellite and in situ measurements. This study presents a new method to estimate the AMOC at 22.5°S based only on available in situ measurements and optimized with the help of satellite altimetry data. This method resolves the energetic Brazil Current (BC) near the western boundary, westward propagating signals, and coastal sea level variability. It is shown that the overturning circulation is stronger during the austral fall/winter and weaker in spring, and its interannual variability is mostly driven by changes in the BC. The deep southward transport at 22.5°S is dominated by two flows along the western and eastern boundaries near 2,500 m depth. Our analysis demonstrates the importance of sustained in situ observations to monitor the state of the AMOC.

1. Introduction

The Atlantic Meridional Overturning Circulation (AMOC) is the zonal integral of the complex three-dimensional circulation, characterized by an upper cell connected to the deep convection in the North Atlantic subpolar region, and a lower or abyssal cell originating in the marginal seas off Antarctica (Broecker, 2003; Buckley & Marshall, 2016). The AMOC controls the meridional transport of heat (MHT), freshwater, carbon, and other properties across the basin and links the timescales of heat uptake and carbon storage (Collins et al., 2019; Conway et al., 2018; Todd et al., 2019). The IPCC projections for the 21st century predict a significant weakening of the AMOC, which would result in global and regional impacts on climate, weather, sea level, and ecosystems (Collins et al., 2019; Fox-Kemper et al., 2021; Lee et al., 2021). Theoretical and climate models suggest that the stability of the AMOC is dependent on the oceanic freshwater budget in the South Atlantic (de Vries

& Weber, 2005; Stommel, 1961; Weijer et al., 2019). Depending on the sign of the freshwater transport into the South Atlantic, the AMOC may present hysteresis behavior, in which a reduced AMOC could be sustained even without an anomalous freshwater forcing (Rahmstorf, 1996; Stommel, 1961). Because the net freshwater transport across 35°S in the South Atlantic is southward (Garzoli et al., 2013), a weakening of the AMOC would increase the freshwater transport into the Atlantic, causing negative feedback to the AMOC recovery (Goes, Murphy, & Clement, 2019). In addition, the intensity of AMOC is one of the main sources of uncertainties in climate model projections (Bellomo et al., 2021), which highlights the importance of sustained observational data for a more robust AMOC predictability. Therefore, the monitoring, hindcasting, and future projections of the AMOC variability are crucial for a better understanding of the Earth system dynamics.

Despite its importance, observations of the AMOC are still limited spatially and temporally (Rhein, 2019). Currently, five observing arrays estimate the AMOC (e.g., Volkov, Smeed, et al., 2023), including two in situ observing arrays in the South Atlantic: the TSAA/Tropical Atlantic Circulation and Overturning—TRACOS (11°S; Herrford et al., 2021; Hummels et al., 2015) and the South AMOC Basin-wide Array—SAMBA (35°S; Kersalé et al., 2020; Meinen et al., 2018). TRACOS uses a total of 5 bottom pressure stations to capture boundary variability on both boundaries of the Atlantic basin, combined with altimetry data to obtain AMOC anomalies at 11°S. Hummels et al. (2015) detected a salinity increase of up to 0.1 psu per decade from the surface to intermediate layers at 5°S and 11°S near the western boundary by comparing observations from two periods, 2013–2014 and 2000–2004. Using reanalysis data, Goes et al. (2014) associated the increase in salinity at intermediate depths to an increase of salty Agulhas Leakage into the Atlantic, due to the strengthening of the westerlies associated with the Southern Annular Mode, similar to the mechanism described in Durgadoo et al. (2013).

The SAMBA array at 35°S established in 2009 revealed strong variability in both the upper and abyssal cells of the AMOC (Kersalé et al., 2020). The AMOC variability at 35°S is greatly influenced by the eastern boundary forcing at an interannual time scale, while the influence of the western boundary is greater at semiannual or shorter time scales (Meinen et al., 2018).

Recent studies have stressed the need for understanding the meridional coherence of the AMOC (e.g., Frajka-Williams et al., 2019; McCarthy et al., 2020). Anomalous signals from the South Atlantic can propagate toward the subpolar North Atlantic and affect deep water formation (Biastoch et al., 2009; Desbruyeres et al., 2021). The AMOC-induced heat and freshwater convergences and divergences drive changes in regional heat and freshwater contents and in sea level (Little et al., 2017; Volkov, Baringer, et al., 2019; Volkov, Lee, et al., 2019; Volkov, Zhang, et al., 2023), which can impact the climate locally (Chang et al., 2008) and remotely (Lopez et al., 2016).

This study aims to establish an AMOC observing system at 22.5°S. A system at this location would bridge the two existing observing systems located at the edges of the South Atlantic subtropical gyre (11°S and 34.5°S) and provide estimates that can be compared to the historical cross-basin hydrographic programs such as World Ocean Circulation Experiment (WOCE) and Global Ocean Ship-based Hydrographic Investigation Program (GO-SHIP) occurring since the early 1990s. However, building new, sustainable observing systems can be a daunting task due to the associated operational and financial costs (Chidichimo et al., 2023). Therefore, an AMOC observing system that relies on existing sustained observations at no additional costs is a strategic opportunity to enhance our understanding of this vital climate component.

Although there are AMOC reconstructions at a few locations in the South Atlantic based on linear regression between satellite altimetry and in situ data (e.g., Dong et al., 2021; Majumder et al., 2016), none of these estimates relies solely on sustained hydrographic data. The AX97 XBT high-density transect near the western boundary centered at about 22.5°S accounts for nearly 100 occupations and, therefore it can serve as a reliable constraint on the variability of the Brazil Current (BC), which is known to have a great influence on the AMOC variability in other locations. In addition, according to Dong et al. (2021), the AMOC time series at 35°S is not correlated with that at 20°S, which suggests different regimes at the two locations, thus analyzing the SAMOC array at 35°S along with an AMOC transect at 22.5°S would allow examining this hypothesis using exclusively direct observations.

With that said, the main objective of this study is to estimate the AMOC and MHT at 22.5°S by merging available in situ ocean observations and atmospheric reanalysis products. We further examine the seasonal and interannual variability of the AMOC and MHT during the 2007–2020 period.

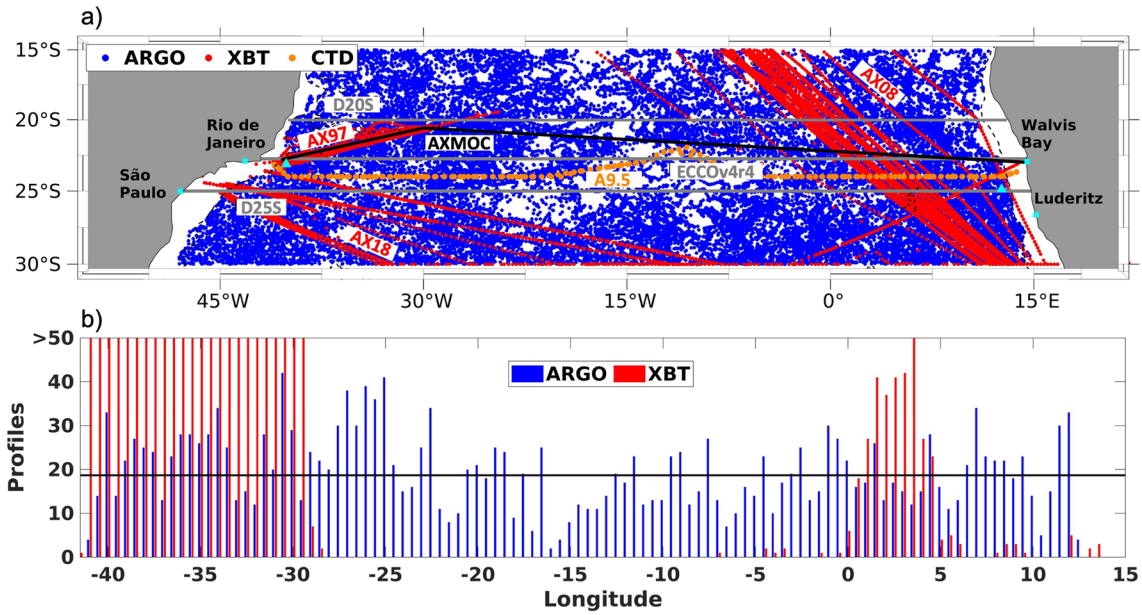

Figure 1. (a) Locations of in situ measurements used in this work and measurements used for comparison and validation. The locations of Argo (XBT) profiles are represented by blue (red) dots, and orange dots represent the location of T-S profiles acquired by CTD casts during Global Ocean Ship-based Hydrographic Investigation Program/CLIVAR cruises along the A9.5 transect in 2009 and 2018. The reference 22.5°S transect (AXMOC) is represented by the black line. The location of coastal tide gauges is represented by cyan squares. The cyan triangles represent the locations of the altimetry data used to compare with the AXMOC dynamic heights near the boundaries. Dashed black lines represent the 1,000 m isobath. Gray lines are the locations of the validation data sets (D20S, D25S, ECCOr4v4). (b) Number of profiles located within a radius of 0.5° from each nominal longitude along the reference transect. Argo profiles are represented in blue and XBT profiles are represented in red. Solid line represents the average number of Argo profiles within a 0.5° radius.

This paper is organized as follows: the in situ and reanalysis data used in this study are presented in Section 2, as well as the method to construct the referenced transect and its AMOC estimate. Section 3 evaluates the proposed method and, presents the AMOC and MHT time series estimates and their different components based on the reference section and other products available in the region. Section 4 summarizes our main findings.

2. Data and Methods

2.1. In Situ Profile Data

Observational data from three high-density eXpendable BathyThermograph (XBT) transects (AX08, AX18, and AX97) and Argo profiling floats in the South Atlantic Ocean are used to build a trans-basin transect near 22.5°S (Figure 1a). The XBT probes measure temperature (T) along fixed transects from surface to depths of about 800 m, and Argo floats measure T and salinity (S) down to 2,000 m. The AX08 transect crosses the Atlantic Ocean from Cape Town (South Africa) to New York (USA), spanning the eastern part of the South Atlantic subtropical gyre. The AX18 transect monitors the AMOC and MHT with two cross-basin zonal transects at approximately 34.5°S, and some of its realizations go further north to ~24°S in the western side of the basin depending on the availability of merchant ships. AX97 monitors the BC near 22.5°S from Rio de Janeiro (Brazil) to Trindade Island (~30°W). The average temporal sampling frequency of the AX08 and AX18 transects is four repetitions/year and for AX97 is 6 repetitions/year. The average horizontal sampling ranges from 18 to 27 km. XBT data are obtained from the NOAA/Atlantic Oceanographic and Meteorological Laboratory (AOML) database (XBT Network, 2021), and profiles of S are derived from XBT-measured T profiles using a seasonal regression method proposed by Goes et al. (2018). Delayed mode Argo profile data (Argo, 2020) are used from the Global Argo Data Repository of the National Centers for Environmental Information (NCEI). Only adjusted Argo T-S profiles flagged as good or potentially good are used. The disparity found in some profiles, for which the available S data were fewer than the T data, was circumvented by applying the same regression method to estimate S from the XBT-measured T profiles.

To complete the profiles for the full water column, that is, below 800 m for XBT data and below 2,000 m for Argo data, the 0.25° horizontal resolution NCEI World Ocean Atlas 2018 (WOA18) T-S climatology is used, at

monthly averages between 800 and 1,500 m, and seasonal averages below 1,500 m (Garcia et al., 2019; Locarnini et al., 2018; Zweng et al., 2019). Monthly WOA18 data have 57 vertical levels from 0 to 1,500 m, and seasonal data have 112 vertical levels from 0 to 5,500 m. Sensitivity tests performed with Argo data showed that the effect of padding from 800 to 1,600 m is negligible relative to uncertainties that arise from the sampling strategies and from the methodologies of heat and volume transports calculation (Goes et al., 2020).

Each T-S profile is linearly interpolated to 140 pre-defined depths levels between 5 m and the maximum depth of 6,000 m, with 10 m intervals between 5 and 745 m, 50 m intervals between 745 and 2,000 m, and 100 m intervals between 2,000 and 6,000 m.

2.2. Auxiliary Data

Monthly zonal wind stress data from the ERA5 atmospheric reanalysis (Hersbach et al., 2020) are used to estimate the Ekman component of the AMOC. ERA5 wind stress data are available at a 0.25° horizontal grid since 1979, and were linearly interpolated to the 22.5°S reference section for the period 2007–2020.

For data validation, comparison, and water mass analysis, we used the Argo T-S 0.5° × 0.5° gridded monthly climatology (RG Argo—Roemmich & Gilson, 2009) from 2007 to 2020, and hydrographic profiles from GO-SHIP which contributes to Climate and Ocean: Variability, Predictability and Change project (GO-SHIP/CLIVAR—Talley et al., 2016). RG Argo climatology data is a gridded product of the upper 2,000 m of the ocean based on a weighted least squares fit to the nearest 100 Argo profiles (Roemmich & Gilson, 2009). RG Argo velocity field was calculated from the thermal wind equation, using a level of reference in 1,000 m and adjusted to the mean Argo parking velocity field from YoMaHa'07 (Lebedev et al., 2007). The GO-SHIP/CLIVAR T, S, and dissolved oxygen data used here are from the transect A9.5 (hereafter A9.5), located close to 24°S from South America to Africa, which were surveyed by two different scientific cruises in 2009 and 2018 (740H20090307 and 740H20180228, respectively). A total of 238 CTD/O_2 stations were collected in those 2 periods, from which 214 of those stations were used in this study (yellow circles in Figure 1a). A9.5 data were interpolated to the same 140 pre-defined depths used in the XBT and Argo profiles. T-S data from the Estimating the Circulation and Climate of the Ocean version 4 release 4 (ECCOv4r4) ocean state estimate were also used, covering the period 1992–2017 at a 0.5° × 0.5° horizontal resolution. This product is an updated version of that described by Forget et al. (2015). Finally, for the mapping calibration and validation of the scattered observations, we use monthly gridded sea level anomaly (SLA) from January 1993 to December 2020 from a multi-satellite altimetry mission, processed and distributed by the Copernicus Marine and Environment Monitoring Service (Pujol et al., 2021). The SLA maps have been previously filtered, bias corrected, and corrected for atmospheric pressure effects and tides using the method of Pujol et al. (2016). The 20-yr mean dynamic topography (Rio et al., 2011) is added to SLA to obtain the sea surface height (SSH) fields. The global mean sea level has risen at a rate of approximately 3.50 mm yr^{-1} over the past 3 decades (Ablain et al., 2019; Volkov, Zhang, et al., 2023). To avoid time varying biases during the mapping optimization phase, linear trends are removed from the fields at each longitude of the reference transect.

2.3. High-Resolution T-S Reference Section Mapping Method

A high-resolution reference section based on Argo and XBT data at 22.5°S, hereafter AXMOC, is defined in order to maximize the data availability along the section. Therefore, on the western side of the basin, the section follows the AX97 XBT transect from Rio de Janeiro to Trindade Island (~30°W), and from 30°W to Walvis Bay in Namibia. Long-record tide gauges are located on both ends of the reference transect (light blue squares in Figure 1a). Data from two other XBT transects, the AX08 and AX18 are used to improve data coverage locally along their tracks. The coverage of Argo profiles is greater where bathymetry is deeper than 1,000 m, and it improved after 2007 in the South Atlantic following the initial spinup of the program in 2004 (Roemmich et al., 2009).

The mapping method used to reconstruct the T and S along the reference section consists of weighted averages (Goes et al., 2010, 2020) using a normalized separable exponential function in space and time, given by:

$$W = \exp\left(-\frac{\sqrt{x^2+y^2}}{\Delta R}\right) * \exp\left(-\frac{\delta t^2}{\Delta t}\right), \quad (1)$$

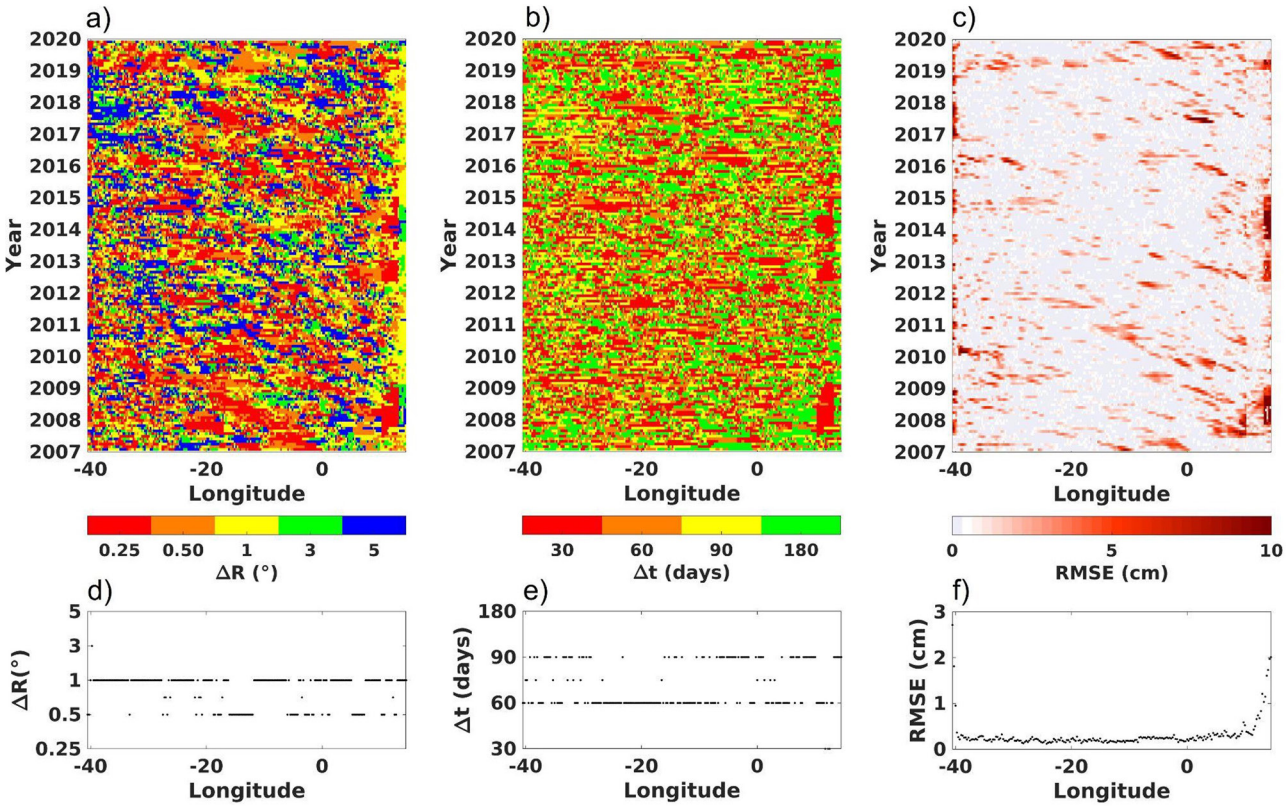

Figure 2. Values of spatial (a) and temporal (b) mapping ranges selected by the minimization of the Root Mean Square Error (RMSE) between DH and sea surface height (c). Median values for each longitude are presented for spatial range (d), temporal range (e) and RMSE (f).

where ΔR is a spatial radius, Δt is a time window, δt is the time difference between the profile and the reference time (fifteenth of each month), and x and y are the zonal and meridional distance between the profile location and the referenced coordinate position, respectively. A set of 20 sections is generated considering a combination of weight values obtained varying ΔR (0.25°, 0.50°, 1°, 3°, and 5° radius) and Δt (30, 60, 90, and 180 days). The search radius at the boundaries (west of 37°W and east of 10°E) was enlarged in the y-direction by a factor of 3 with a cut off of 5° to minimize data gaps, assuming the features are more coherent along the boundaries than across (Figure S1 in Supporting Information S1).

The optimal T-S section was obtained by optimizing the mapping parameters ΔR and Δt locally by minimizing the root mean squared error (RMSE; used as a cost function) between absolute dynamic height (DH) and the SSH data interpolated to the reference section (Figure 2). The absolute DH of each parameter subset was referenced to 1,000 m, and the absolute geopotential field from a blended Argo/altimetry climatology product was added to the reference level (Goes, Cirano, et al., 2019). During calibration, both data were detrended in time to avoid misfits due to the mass and barotropic components of the variability in altimetry data.

The optimal parameters ΔR and Δt are generally noisy (Figures 2a and 2b), which reflects the variable data coverage along the section. Small differences in the RMSE can also influence the choice of the mapping parameters, and contribute to this variability. A possible solution to this issue would be to include a prior probability distribution in the parameters, so smaller ΔR and Δt values would receive slightly more weight, normalizing small differences in RMSE (e.g., Goes et al., 2010). Sensitivity experiments (not shown) suggest that the impact of this approach in the final AMOC and MHT time series is small (RMSE up to 1 Sv for AMOC estimates and up to 0.1 PW for MHT estimates), even for higher ΔR and Δt values, since our method provides a greater weight to data closer in time and space to the referenced transect at a given time (Equation 1). The median ΔR (Δt) values fall between 0.50° and 1° (60 and 90 days) for every point of longitude (Figures 2d and 2e). The median RMSE between the absolute DH and SSH is 0.79 ± 1.40 cm, and increases to ∼2 cm in the eastern boundary (Figure 2f). These values fall well within previously published RMSE values of 6.2 cm for areas between 5°S and 15°S, and up to 14 cm at the boundaries (Arnault et al., 1992; Strub et al., 2015).

2.4. AMOC and MHT Time Series

The AMOC and MHT across the reference section are calculated following published methodologies for the South Atlantic (e.g., Dong et al., 2015, 2021; Goes et al., 2015, 2020). The AMOC is defined as:

$$\Psi_y(z) = \int_{x_E}^{x_W} \int_{-H}^{z} v(x, z) dx dz, \tag{2}$$

where the AMOC stream function across a zonal section (Ψ_y) is the integral of the meridional velocity $v(x, z)$ (adjusted to ensure zero net volume transport across the section) from the bottom (H) to depth (z) and between the western (x_W) and eastern (x_E) boundaries.

The MHT is defined as:

$$\text{MHT} = \rho_0 c_p \int_{x_E}^{x_W} \int_{-H}^{0} v(x, z)\theta(x, z) dx dz, \tag{3}$$

where ρ_0 is the mean water density (1,025 kg m^{-3}), c_p is the specific heat of the sea water (4,187 J kg^{-1} K^{-1}), and θ is the potential temperature along the section.

The AMOC and MHT are divided into geostrophic and Ekman components. The geostrophic velocity field is computed from the thermal wind equation, using the gridded T-S data, and adopting 3,700 m as reference level, as it is approximately the depth of the neutral density $\gamma = 28.1$ kg/m^3, usually considered as the boundary between North Atlantic Deep Water (NADW) and Antarctic Bottom Water (AABW) at 22.5°S (see Section 3.3). This reference depth is similar to the one defined for 34.5°S (Goes et al., 2015). A zero net volume transport constraint is applied to the section at each month by adjusting the velocity field with a constant, calculated from the integrated transport across the section divided by the area of the section. This method is a classical approach to estimate AMOC and MHT (e.g., Dong et al., 2015, 2021; Goes et al., 2015, 2020). However, inverse models are also widely used to calculate the AMOC (e.g., Arumí-Planas, et al., 2023; Caínzos et al., 2022; Hernández-Guerra et al., 2010; Lux et al., 2001). The geostrophic AMOC stream function is estimated from the adjusted velocities (v, Equations 2 and 3), and its strength is defined as the maximum value of the stream function at each timestep. The Ekman component, estimated using the ERA5 reanalysis, is integrated to the depth of the Ekman layer, which is considered to be 50 m deep. Both the AMOC and MHT represent the sum of Ekman end geostrophic components. The time series of the AMOC and MHT span from 2007 to 2020, since the AX97 transect started in 2004 and the Argo data have been more widely available across the South Atlantic basin since 2007.

3. Results

In this section, sea level, boundary currents, and water mass characterization are presented to evaluate the AXMOC product. The AMOC and MHT time series are decomposed into the seasonal, interannual (low-pass filtered with a 13-month Gaussian), as well as Ekman and geostrophic components.

3.1. Sea Level

Here, the SLA calculated along the AXMOC transect from 2007 to 2020 is compared with those obtained from satellite altimetry and the RG Argo data (Figure 3). It is important to emphasize the AXMOC is uniquely based on in situ observations, and altimetry data is used only for the optimization of our mapping parameters. Therefore, AXMOC data can be considered independent from altimetry and the study differs from previous studies that used direct statistical relationships between in situ and altimetry data (e.g., Dong et al., 2015, 2021; Majumder et al., 2016).

Westward propagating signals are readily observed with satellite altimetry. These signals take between 2 and 4 years to cross the basin from east to west, generally without significant energy loss along their path, showing the importance of wave generation near the eastern boundary. An average phase speed of 5.9 ± 1.6 km/day is estimated for this propagation following the method of Barron et al. (2009), which corresponds to the period of the first baroclinic Rossby wave mode near 22.5°S (Polito & Liu, 2003). This westward propagation is not seen in the RG Argo product due to a rather coarse spatial and temporal mapping resolution. Nevertheless, our optimized

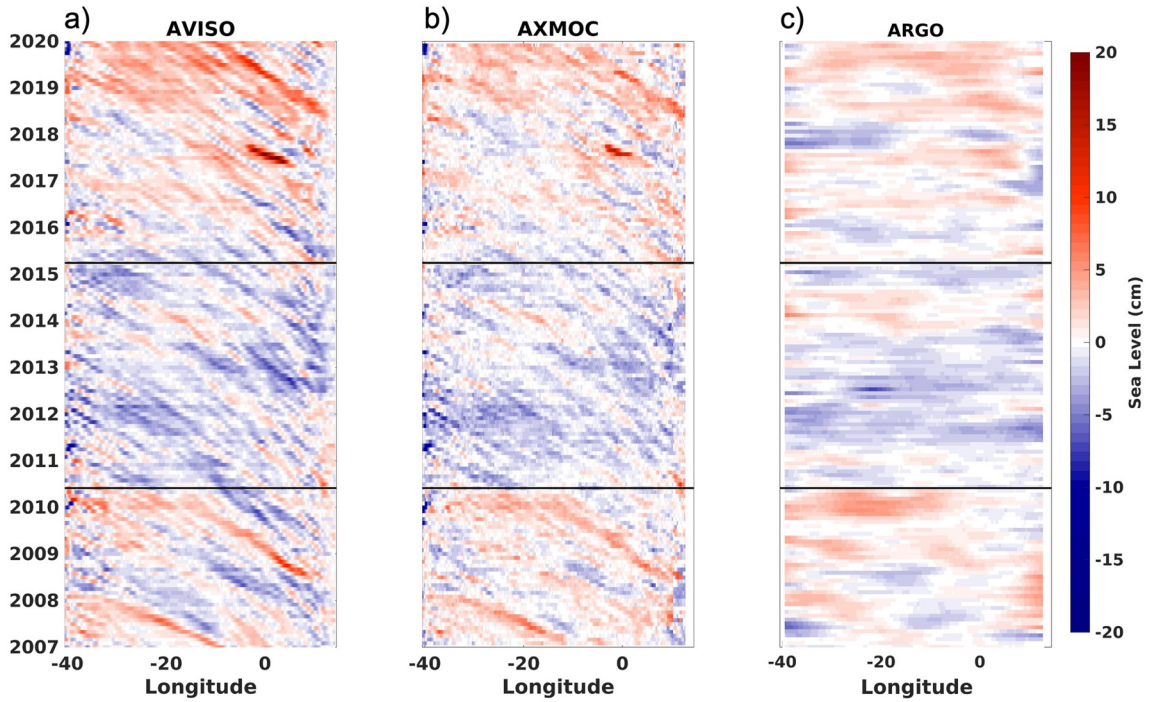

Figure 3. Hovmoller plot of the sea level obtained by altimetry (a), AXMOC (b) and RG Argo (c) data sets. Black horizontal lines indicate dates of June/2010 and April/2015. All data sets are de-seasoned and detrended to focus on the interannual variability.

mapping method allows a reliable detection of these propagation patterns, in a good agreement with satellite altimetry data (Figures 3a and 3b). Although expected, since the mapping parameters are optimized using satellite data, this result provides evidence that the current data distribution of XBT profiles and Argo floats can successfully identify westward wave propagation in the South Atlantic basin.

A basin-wide, multi-year SLA pattern is observed in all three products, characterized by positive anomalies from January/2007 to June/2010, negative between July/2010 and April/2015, and again positive from May/2015 to December/2020 (Figure 3). Although interesting, the analysis of this variability pattern is not within the scope of this study and it is left for future research.

The proposed mapping method (AXMOC) also adequately reproduces the strong SLA variability near the boundaries, particularly near the western boundary due to the higher density of XBT data in the region. Near the eastern boundary, both satellite altimetry and AXMOC products capture some strong SLA signals, such as the negative anomalies in 2012–2013 and the positive anomalies in 2008–2009, 2017, and 2018–2019.

The comparison of SLA time series from satellite altimetry and the AXMOC data near the western (40°W) and eastern boundaries (12.5°E) also validates the proposed method and provides valuable insight on the variability of boundary currents (Figure 4). As satellite SSH has contributions other than steric sea level, particularly in coastal areas, we selected for the boundary sea level height comparison with AXMOC the location of the satellite altimetry time series with higher correlation within 3° from the boundaries. The selected locations for the altimetry product are 40.12°W, 23.12°S (western boundary), and 12.62°E 24.87°S (eastern boundary), shown in light blue triangles in Figure 1. Overall, the standard deviation (used as a proxy of variability) of the SSH is higher near the western boundary (5.7 cm) relative to the eastern boundary (3.4 cm) (Figures 4a and 4b; respectively). The AXMOC data show similar values to SSH near the western (4.9 cm) and eastern (3.1 cm) boundaries.

A good correlation of sea level from AXMOC with altimetry data was obtained at both boundaries (0.89 at the western and 0.84 at the eastern boundary). When considering the de-seasoned sea level anomalies, the correlation at both boundaries remained robust (0.82 for the western and 0.72 for the eastern boundary). Most of the SLA extreme events that arise in the altimetry data also appeared in the AXMOC data (e.g., extreme values at the end of 2009, 2011, 2016, and end of 2019 at the western boundary, and the extreme values early 2010, mid 2012 and

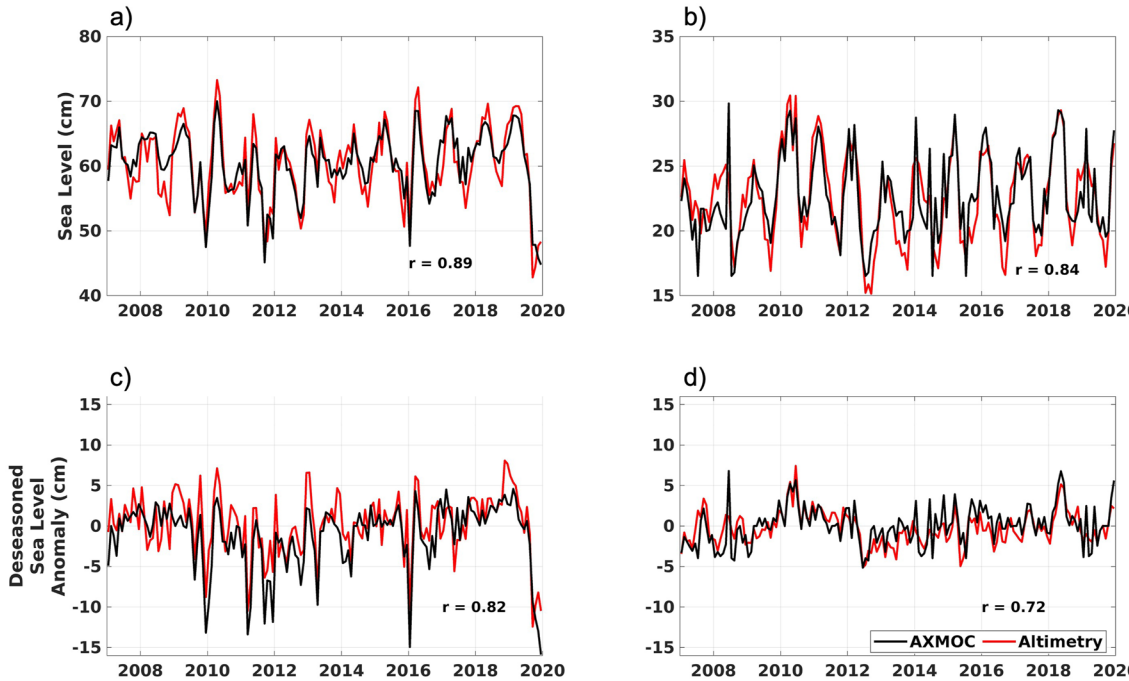

Figure 4. Absolute (a) and (b) and de-seasoned (c) and (d) sea surface height at the western (a) and (c) and eastern (b) and (d) boundaries of the section. Red is for altimetry data, and black is for the AXMOC estimates. The associated correlation values are shown in each panel.

mid 2018 at the eastern boundary). As expected, robust correlations were observed at both ends of the section, even though the eastern boundary is only sparsely sampled by Argo floats. On the other hand, the western boundary is densely sampled by XBTs and thus better constrained. This indicates that the use of a sea level-oriented mapping method is appropriate to monitor the evolution of near-coastal features.

3.2. Boundary Currents

Here, we compare boundary currents derived from the AXMOC with those derived from the RG Argo and simulated by the ECCOv4r4 state estimate. At 22.5°S, the BC is a shallow and narrow southward flow along the Brazilian coast placed on top of the northward inflow of the Intermediate Western Boundary Current (IWBC) (Calado et al., 2008). In the AXMOC data, the mean BC is located west of 39°W in the top 500 m (Figure 5b). In the RG Argo, the BC is constrained to the west of 39.75°W, and a strong northward core appears east of 39.75°W, which is an artifact caused by the reverse DH gradient created from the lack of in situ data near the western boundary (Figure 1b blues bars west of 40°W; Goes et al., 2020). In ECCOv4r4, the BC appears shallower and wider (west of 38°W) than in the AXMOC data. To analyze its volume transport in the three data products, we define the BC as the southward flow in the upper 500 m between the western boundary and 38°W. The 10-year (2007–2017) averaged and standard deviation of the volume transport is slightly higher, but not statistically different, (-3.64 ± 1.94 Sv) for the AXMOC, compared to -2.64 ± 0.77 Sv for the RG Argo and -3.23 ± 1.03 Sv for the ECCOv4r4. The mean BC core speed is also slightly higher, but not significantly different, in the AXMOC data (-0.19 ± 0.10 m s^{-1}) than in the RG Argo (-0.16 ± 0.04 m s^{-1}) and ECCOv4r4 data (-0.10 ± 0.02 m s^{-1}). Previous regional studies report a mean BC volume transport varying between -2.3 and -4.8 Sv, with a standard deviation that is frequently higher than its mean value (da Silveira et al., 2008; Lima et al., 2016; Mata et al., 2012; Pereira et al., 2014; Pita et al., 2020). Therefore, it is reasonable to consider that the AXMOC data can represent the variability of the BC transport, producing a standard deviation almost twice as large as the RG Argo and ECCOv4r4 products. The greater variance of the AXMOC volume transport estimate is caused by better resolution of BC interannual variability, which captures the strong event in the summer of 2009/2010, analyzed in Goes, Cirano, et al. (2019), as well as other events such as 2014 and 2016, which were also observed in that study. This interannual variability is dampened in the other two products.

Close to 22°S, the Benguela Current (BeC) is the eastern boundary current, which flows equatorward between the coast to 3°E, limited by the Walvis ridge (Garzoli & Gordon, 1996; Majumder & Schmid, 2018). The AXMOC

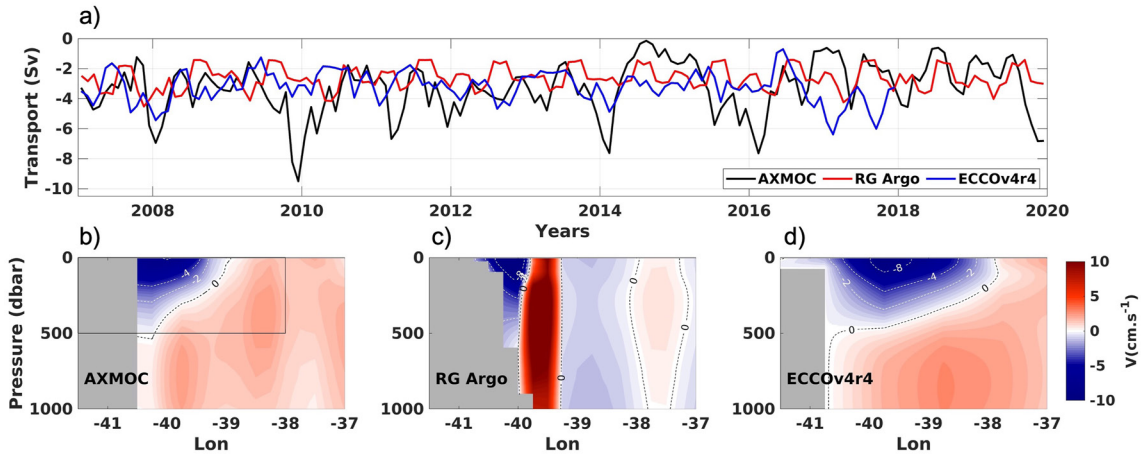

Figure 5. Evolution of the Brazil Current (BC) transport from three different data (a): AXMOC (black line), RG Argo (red line) and ECCOv4r4 (blue line). Mean velocity section focused on western boundary is shown for AXMOC (b), RG Argo (c), and ECCOv4r4 (d) data sets. The black rectangle in (b) indicates the region where the BC transport is being calculated.

data capture the BeC as an equatorward flow from surface down to 500 m with a core located between 10 and 12°E (Figure 6b). The poleward flow east of 12°E is the expression of the Poleward Undercurrent, an ocean current derived from the sinking of the Angola Current at the Angola Benguela Frontal Zone (Berger et al., 1998). On the other hand, the RG Argo data show a strong equatorward flow along the edge of continental shelf, due to the lack of data near the coast (Figure 6c). The BeC transport of 12.57 ± 2.58 Sv observed in AXMOC is similar to the one observed in RG Argo (11.05 ± 2.09 Sv) and greater than ECCOv4r4 data (3.43 ± 0.68 Sv). AXMOC data perceive a more intense and variable BeC compared to the other products. The low resolution of ECCOv4r4 produces a weaker and less variable BeC transport, and a smoother BeC structure (Figure 6d) which is significantly different from the AXMOC and RG Argo estimates. The AXMOC results are in accordance with Majumder and Schmid (2018), which also reported a decreasing mean BeC volume transport on lower latitudes, varying from 23 Sv at 31°S to approximately 9 Sv at 25°S.

3.3. Water Masses

This subsection analyzes the water masses along the AXMOC data, and compares its results with independent in situ data from A9.5 transect. The trans-basin section at 22.5°S is characterized by more intense circulation on both boundaries in comparison to the interior of the section (Figure 7a). Most of the variability along the section is concentrated in the upper ocean and near the boundaries (Figure 7b).

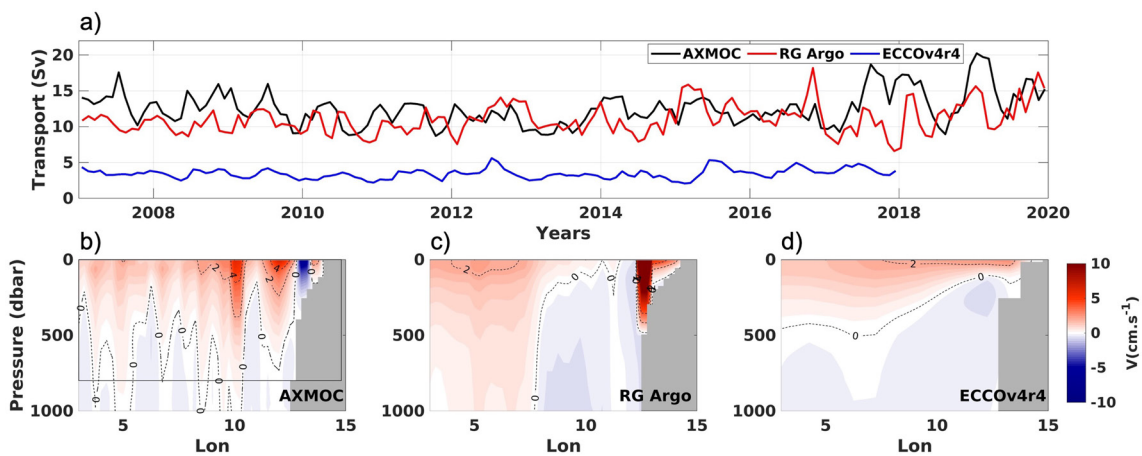

Figure 6. Evolution of the Benguela Current (BeC) transport from 3 different data (a): AXMOC (black line), RG Argo (red line), and ECCOv4r4 (blue line). Mean velocity section focused on the eastern boundary is shown for AXMOC (b), RG Argo (c), and ECCOv4r4 (d) data sets. The black rectangle in (b) indicates the region where the BeC transport is being calculated.

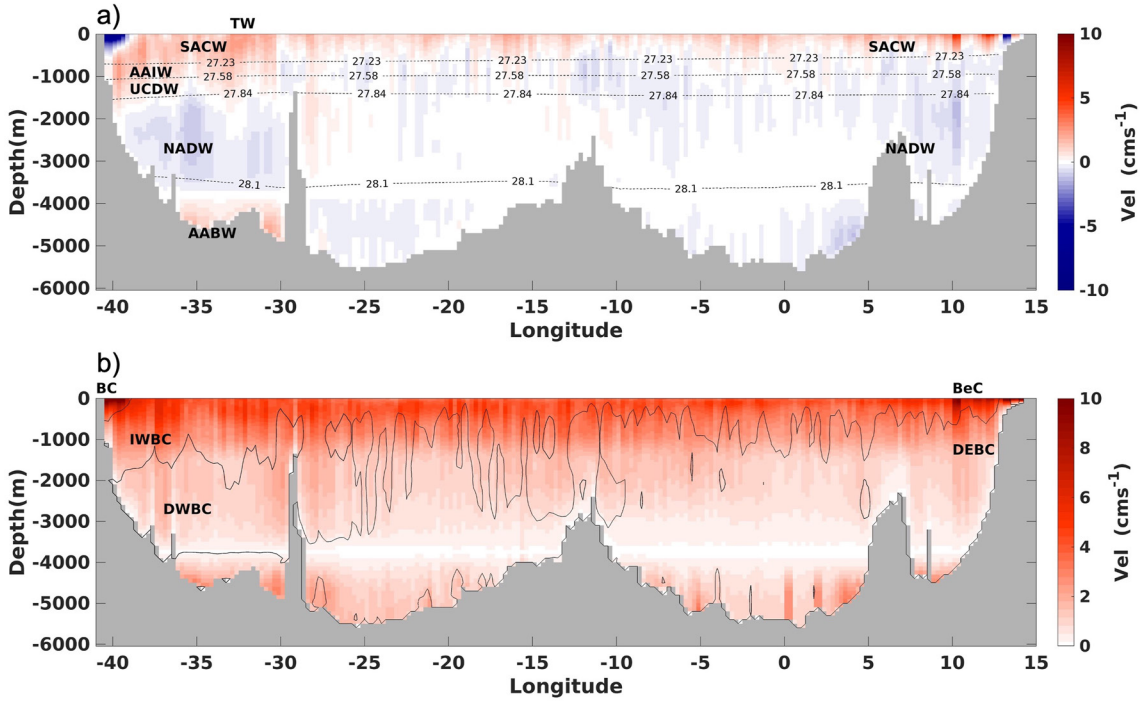

Figure 7. Mean northward velocity at 22.5°S (a) and its standard deviation (b) computed from the AXMOC data. The main water masses (a) and ocean currents (b) are indicated: Tropical Water, South Atlantic Central Water, Antarctic Intermediate Water, Upper Circumpolar Deep Water, North Atlantic Deep Water, Antarctic Bottom Water , Brazil Current, Benguela Current, Intermediate Western Boundary Current, Deep Western Boundary Current and Deep Eastern Boundary Current. Neutral density isopycnals are represented by dashed lines in (a). Solid lines in (b) indicate contour of no meridional velocity.

At 22.5°S, the AXMOC velocities show most of the AABW flow below 4,000 m, confined by the Trindade Island topography to the west of 30°W, and with core speed of 0.02 ± 0.01 m s^{-1} (Figure 7a). The AABW is characterized by T < 2°C, S < 34.8 and reduced dissolved oxygen levels (O_2 ≃ 220 μmol kg^{-1}) relative to NADW (Figures 8a–8c, 8e, and 8f and Figure S2 in Supporting Information S1), which is in agreement with Reid (1989). Between 50°S and the equator, the AABW flows along neutral density lines γ > 28.10 kgm^{-3} (Liu & Tanhua, 2021).

Similar to the AABW, the NADW is also confined by local topography near the western boundary. Near the eastern boundary (Figure 7a), a secondary southward NADW branch is also visible. Indeed, the NADW has been reported to split into two branches before crossing 22°S: one branch remains flowing southward near the western boundary and another branch flows eastward along the equator (Talley, 2011). Both branches are located between 1700 and 3,600 m, and the western branch is more intense, reaching up to −0.01 ± 0.01 m s^{-1} at 22.5°S (Figure 7a). In the tropics, the NADW is usually divided vertically into the upper (uNADW) and lower NADW (lNADW—Talley, 2011) cores. As it flows southward, vertical mixing slowly merges this two-lobed water mass into one main core flowing between neutral density surfaces of 27.84 and 28.10 kg m^{-3} (e.g., Hernández-Guerra et al., 2019; Liu & Tanhua, 2021; Stramma et al., 2004). This single core signal is observed on both branches of the NADW (Figure 7a), which is characterized by a local maximum in salinity (S > 34.85) and a maximum in dissolved oxygen (O_2 > 240 μmol kg^{-1}) near the western boundary (Figures 8b, 8c, and 8f). On the Eastern boundary (Figure S2 in Supporting Information S1), the NADW is slightly less salty than the Western boundary NADW (Figures S2a and S2b in Supporting Information S1) and the local maximum in dissolved oxygen is less prominent (O_2 > 220 μmolkg^{-1}; Figures S2c and S2d in Supporting Information S1). Hernández-Guerra et al. (2019) also reported a difference in NADW salinity on both boundaries in the South Atlantic. This difference likely arises from the interaction between the NADW crossing the basin and the southward currents along the eastern boundary (Garzoli et al., 2015).

The Upper Circumpolar Deep Water (UCDW) is defined as a fresh (core S around 34.6), low oxygen water mass with neutral density between 27.58 and 27.84 kg m^{-3} and located between 1,150 and 1,550 m deep (e.g., Hernández-Guerra et al., 2019). It is characterized by low salinity (S < 34.8) and poor oxygen levels

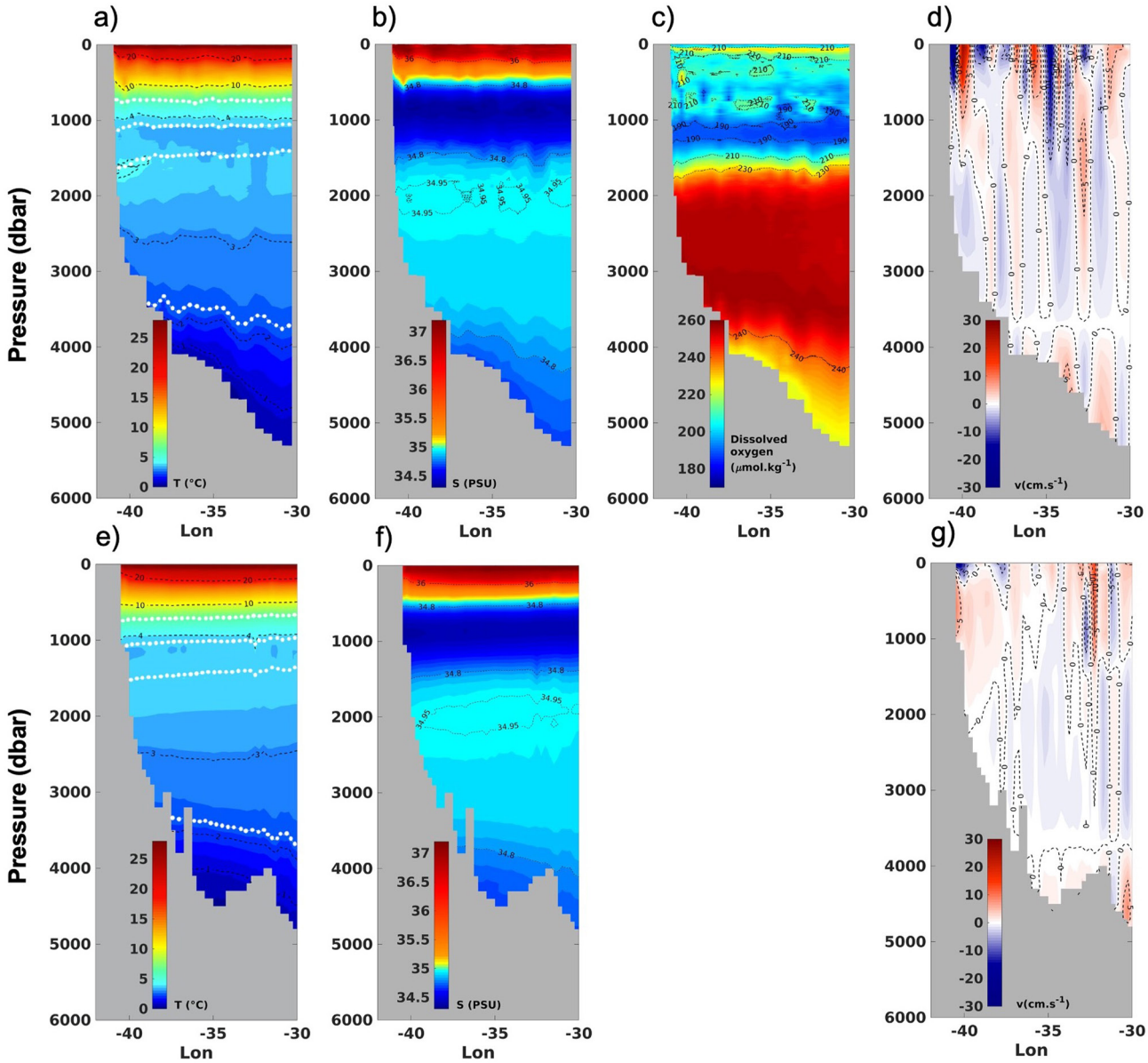

Figure 8. Ocean tracers and velocity section focused on western boundary for March 2018 at 24 and 22.5°S. A-d (e–g) panels represent A9.5 (AXMOC) data. Temperature (T), salinity (S), dissolved oxygen and velocity (v) are shown between western boundary and 30°W. Black dashed lines represent: (i) isotherm of 1, 2, 3, 4, 10, and 20°C (a, e); (ii) isohaline of 34.8, 34.95, and 36 (b, f); (iii) lines of same dissolved oxygen of 190, 210, 230, and 240 μmol kg^{-1} (c) and (iv) increments of 5 cm/s (d, g). White dotted lines in (a) and (e) represent neutral density isopycnal of 27.23, 27.58, 27.84, and 28.10 kg m^{-3}.

(O_2 < 190 μmol kg^{-1}; Figures 8b, 8c, and 8f). Located above the UCDW, at depths varying from 700 to 1,150 m, the Antarctic Intermediate Water (AAIW) is characterized by a minimum salinity at its core (S < 34.5) located around 800 m, and relatively high oxygen levels, flowing along neutral densities between 27.23 and 27.58 kg m^{-3}. Both UCDW and AAIW form the Intermediate Western Boundary Current system (IWBC) at 22.5°S (Figure 7a), which is characterized by an equatorward flow near 38°W between about 600 and 1,700 m depth (Figure 7a).

The isolines of T, S in the AXMOC and A9.5 data are located at similar depths (Figures 8a, 8b, 8e, and 8f). The isolines of the A9.5 data are more variable, while the AXMOC isolines are smoother. This is because the AXMOC is based on time and space averaging applied during the mapping procedure, and the A9.5 data are based on unsmoothed CTD casts. The same comparison holds for the 2009 A9.5 occupation (not shown).

A direct comparison of volume transport in neutral density intervals is an important step in evaluating the mapping method applied here (Figure 9). While AXMOC and A9.5 AMOC estimates are calculated from their

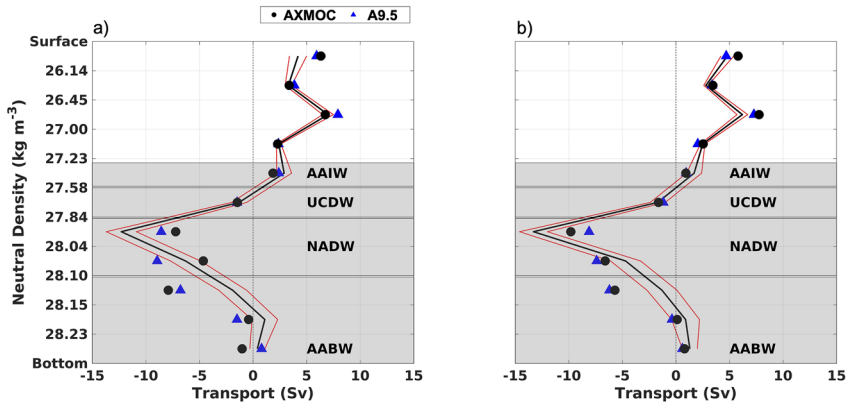

Figure 9. Volume transport at different neutral density levels for two different months: April/2009 (left panel) and March/2018 (right panel). AXMOC data are represented by black circles and A9.5 data by blue triangles. Black line and red lines represent the volume transport and its uncertainties estimated by the inverse model of Caínzos et al. (2022) for the decades of (left) 2000s and (right) 2010s decades. The gray areas represent the density ranges of the main water masses across the section: Antarctic Intermediate Water, Upper Circumpolar Deep Water, North Atlantic Deep Water and Antarctic Bottom Water.

respective T-S profiles, Caínzos et al. (2022) employ an inverse box model to compute decadal AMOC estimates from various WOCE/GO-SHIP/CLIVAR transects. The top layer (from surface to $\gamma = 26.45$ kg m^{-3}) is composed by the geostrophic transport and the Ekman transport, while the remaining intervals are composed solely of the geostrophic transport. A good agreement exists between AXMOC and A9.5 volume transport estimates in the upper 1,000 m, characterized by $\gamma < 27.58$ kg m^{-3}. The AXMOC data show a transport of 20.60 and 20.48 Sv for April/2009 and March/2018, respectively. The volume transports in the A9.5 data are 22.78 and 18.95 Sv for April/2009 and March/2018, respectively. The difference between the A9.5 and the AXMOC data in the upper ocean ($\gamma < 27.58$ kg m^{-3}) is generally within the uncertainty interval estimated by Caínzos et al. (2022).

The area encompassing upper layer boundary currents ($\gamma < 27.23$ kg m^{-3}), that is, BC and BeC, has a positive net volume transport of 18.74 and 19.55 Sv for April/2009 and March/2018, respectively ($\gamma < 27.23$ kg m^{-3}, black circles in Figure 9). For A9.5 data, the volume transports are 20.34 and 17.89 Sv for April/2009 and Mar/2018, respectively. AXMOC and A9.5 results are similar in every level for both periods analyzed (April/2009 and March/2018), and this similarity is also observed with the decadal results from Caínzos et al. (2022). At 22.5°S, the upper AMOC cell is located from surface to $\gamma = 27.58$ kg m^{-3}, and the lower AMOC cell is located from $\gamma = 27.58$ kg m^{-3} to the bottom. Considering the layer encompassing the UCDW, the resulting AXMOC-based transports are slightly negative −1.47 and −1.62 Sv for April/2009 and March/2018, respectively ($27.58 < \gamma < 27.84$ kg m^{-3}, black circles in Figure 9), because the more intense intermediate equatorward currents are limited to the western boundary, while the interior and eastern boundary have poleward flow (Figure 7a). In both periods analyzed, the NADW is the main conduit of the lower AMOC cell from neutral density of 27.84–28.10 kg m^{-3} (Figure 9 $27.84 < \gamma < 28.10$ kg m^{-3}). Finally, in the AABW, the resulting transport turns back northward. The mapping method is robust considering that most of its estimates fall within 2 times the uncertainty levels of the independent study performed by Caínzos et al. (2022), especially in the upper ocean. It is important to highlight that both sections, AXMOC and A9.5 (also used as reference in Caínzos et al., 2022), are not located at the same latitude. A9.5 section is located around 24°S and AXMOC transect location varies between 20.5 and 23°S. Greater differences between AXMOC, A9.5, and Caínzos et al. (2022) are observed in areas with $\gamma > 27.84$ kg m^{-3}, because of uncertainties inherent in the method and use of WOA18 climatology data in the AXMOC section in areas without XBT and Argo observations.

3.4. AMOC and MHT Time Series

In this subsection, the newly produced AMOC and MHT time series from AXMOC data are presented along with their contributions from geostrophic and Ekman components. The correlations of AMOC and MHT with each component and with estimates from other data sets are discussed in the supplementary material (Figures S3–S5 in Supporting Information S1). Finally, the influence of western and eastern boundaries, and the interior region of the ocean is addressed.

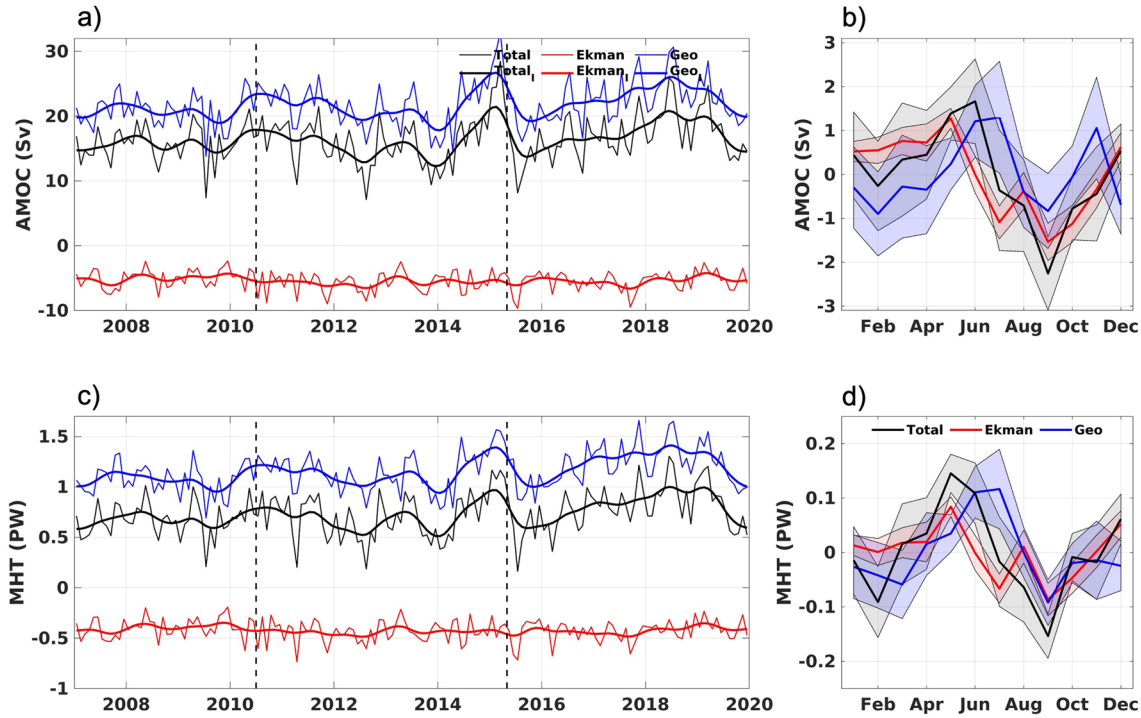

Figure 10. Atlantic Meridional Overturning Circulation (AMOC) and Meridional Heat Transport (MHT) time series (left) and associated seasonal cycles (right). AMOC (a, b) and MHT (c, d) time series are divided into geostrophic (blue lines), Ekman (red lines) and total components (black lines). Solid lines represent the 13-month Gaussian filtered component of AMOC and MHT (a, c, respectively). Vertical black dashed lines (a, c) indicate dates of June/2010 and April/2015, the dates of noticeable changes in sea level anomaly (Figure 3). Shaded areas in black, blue and red represent the standard error of the climatology for the total, geostrophic and Ekman components of the AMOC (b) and MHT (d) respectively.

3.4.1. Mean and Seasonal Cycle

The estimated mean AMOC (MHT) transport from AXMOC data is 16.3 ± 3.2 Sv (0.7 ± 0.2 PW) between 2007 and 2020. In situ estimates at 24°S (A9.5) capture the total AMOC strength of 21.5 Sv (Bryden et al., 2011) and 17.5 ± 0.9 Sv (Arumí-Planas et al., 2023) during 2009 and 2018, respectively. The total AMOC (MHT) transport from AXMOC is composed by an intense equatorward geostrophic transport of 21.7 ± 2.9 Sv (1.2 ± 0.2 PW) and a significant opposite AMOC (MHT) Ekman component of −5.4 ± 1.5 Sv (−0.4 ± 0.1 PW—Figure 10 and Table 1). On a seasonal time scale, the AMOC is stronger between May and June and weaker in September, and the MHT is more intense in May and weaker in September (Figure 10).

A comparison of the AMOC and MHT time series between the AXMOC, Dong et al. (2021) and the ECCOv4r4 products (Text S3–S5, Figures S3–S5 in Supporting Information S1) suggests that their seasonal variations have similar patterns among these products, with positive values from April to July and negative values between

Table 1
Mean and Std Values for Atlantic Meridional Overturning Circulation (Sv) and Meridional Heat Transport (PW) Between 2007 and 2019

	Total		Geostrophic		Ekman	
	AMOC (Sv)	MHT (PW)	AMOC (Sv)	MHT (PW)	AMOC (Sv)	MHT (PW)
AXMOC	16.3 ± 3.2	0.72 ± 0.20	21.7 ± 2.9	1.15 ± 0.17	−5.4 ± 1.5	−0.42 ± 0.10
D20S	16.6 ± 2.1	0.62 ± 0.17	22.7 ± 1.5	1.20 ± 0.09	−6.3 ± 1.7	−0.58 ± 0.14
D25S	19.3 ± 2.2	0.68 ± 0.17	23.0 ± 1.6	1.01 ± 0.12	−3.7 ± 1.4	−0.33 ± 0.13
ECCOv4r4	14.1 ± 2.6	0.48 ± 0.16	19.1 ± 1.8	0.87 ± 0.10	−5.0 ± 1.4	−0.39 ± 0.10

Note. Total, geostrophic and Ekman components are represented in separated columns.

Table 2
Atlantic Meridional Overturning Circulation Variance Explained by Its Geostrophic/Ekman Components

	AXMOC	D20S	D25S	ECCOv4r4
Geostrophic	0.83 (0.77)	0.41 (0.33)	0.60 (0.44)	0.51 (0.58)
Ekman	0.17 (0.23)	0.59 (0.67)	0.40 (0.56)	0.49 (0.42)

Note. The MHT variance explained by its geostrophic/Ekman components is presented in parenthesis.

August and October (Figure S4 in Supporting Information S1). Overall, the mean values from AXMOC are within the uncertainty ranges of the other products for both AMOC and MHT (Table 1 and Figure S3 in Supporting Information S1). Correlations between AXMOC and individual products are higher for the MHT than for the AMOC: $r = 0.59$ (D20S), $r = 0.51$ (D25S), and $r = 0.44$ (ECCOv4r4) for the MHT and $r = 0.40$ (D20S), $r = 0.35$ (D25S), and $r = 0.29$ (ECCOv4r4) for the AMOC. This relatively low correlation between the AXMOC and the other data sets can be related to the amount of variance explained by the geostrophic component of the AMOC/MHT. The variances explained by the geostrophic and Ekman components of the AMOC are similar in Dong et al. (2021) and in the ECCOv4r4 data, approximately 40%–60% for each component (Table 2). For the AXMOC, however, the geostrophic component is responsible for most (83%) of the total transport variance. The geostrophic component can also explain the stronger variability of the AMOC/MHT in the AXMOC time series (Table 1).

3.4.2. Interannual Variability

The low-pass filtered geostrophic component (blue curves in Figures 10a and 10c) exhibits a strong correlation with the total component (black curves in Figures 10a and 10c) for both AMOC ($r = 0.96$) and MHT ($r = 0.97$). In contrast, the correlation between the low-pass filtered Ekman component and the total component is weaker for AMOC ($r = 0.21$) and MHT ($r = 0.16$). This suggests that the majority of the AMOC and MHT variability in the interannual band can be attributed to the geostrophic transport. In addition, AMOC and MHT transports are highly correlated at 22.5°S ($r > 0.95$) in the total, geostrophic and Ekman components, indicating a dominance of velocity variability over temperature variability in the MHT time series, as was also suggested in other studies in the North and South Atlantic (Dong et al., 2009, 2015, 2021; Johns et al., 2011). Also, the AMOC decreases significantly during intense BC events (Figure 4), as observed during years 2011, 2014, 2015, and 2019 (thin black curve in Figure 10a).

Previous studies indicate that the dominance of geostrophic and Ekman components on the AMOC varies at different latitudes in the South Atlantic. At 20°S, the Ekman component dominates the AMOC variability, while at 25°S, a greater contribution of the geostrophic component is reported (Dong et al., 2015). At 35°S, the relative dominance of Ekman and geostrophic components on the AMOC and MHT alternates throughout the time (Dong et al., 2015, 2021). Results from AXMOC transect agree with D25S estimates (Dong et al., 2015, 2021) on the dominance of the geostrophic component over the Ekman contribution for AMOC and MHT transports. The variability observed in the AXMOC time series appears to have changed since 2014, driving an increase in the AMOC by approximately 2 Sv, possibly due to an interannual to decadal variability strengthening (Figure 10). Dong et al. (2021) also observed a moderate interannual AMOC increase at 25°S (D25S) in both total and geostrophic transports but only after 2017 (Figure S5 in Supporting Information S1). Due to the short extent of our time series, we cannot draw any conclusion about the long term changes of the AMOC. Next, we will compare AXMOC time series with the decadal estimates of Caínzos et al. (2022), Dong et al. (2021) and ECCOv4r4, analyzing them in a decadal perspective.

3.4.3. Decadal Perspective

Applying the same technique used on the AXMOC, we estimate the AMOC transport for the two A9.5 repetitions, April/2009 and March/2018 to be 22.0 and 18.6 Sv, respectively. The corresponding AMOC transports from the AXMOC data are 24.8 and 20.0 Sv. The AXMOC estimates differ from A9.5 estimates by +2.8 Sv and −1.4 Sv, respectively. Therefore, we estimate the mean error due to spatial mapping and data availability to be of ∼2 Sv. To compare the decadal values of AXMOC to the other products, we used the 2010–2019 mean AMOC. The AXMOC mean of 2010–2019 AMOC value is 17 ± 3 Sv, in comparison to 16 ± 2 Sv (D20S), 19 ± 2 Sv (D25S), 14 ± 2 Sv (ECCOv4r4), and 18 ± 1 Sv for Caínzos et al. (2022) inverse model. All but ECCO4v4 mean AMOC are within 2 Sv difference from AXMOC. Relative to the previous decade, the 2010–2019 values exhibit a slight increase (0.2 Sv) in 25°S (D25S) and a slight decrease (−0.6 Sv) in 20°S (D20S), whereas ECCOv4r4 and Caínzos et al. (2022) estimates show stronger AMOC decreases (−1.2 and −1.6 Sv, respectively) between the two periods. Caínzos et al. (2022) also estimated similar differences (−1.5 Sv) for the AMOC at the 1990–1999 decade, from which they reported no significant changes observed in the AMOC near 22.5°S over the past three decades. Given the magnitude of the uncertainties, no significant AMOC changes are observed near 22.5°S over the past two decades observed in the analyzed products.

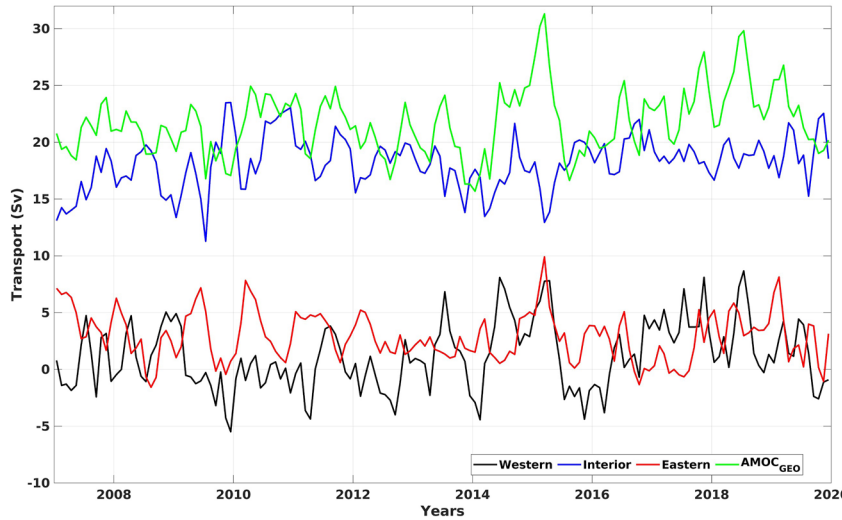

Figure 11. Upper 1,000 m volume transport for western boundary (black), eastern boundary (red) and interior (blue) from the AXMOC data. The geostrophic Atlantic Meridional Overturning Circulation transport is shown by a green line.

3.4.4. Boundary and Interior Contributions

Finally, to understand how the specific areas of the AXMOC transect influence the AMOC at 22.5°S, we compare its geostrophic component to the transport in the upper 1,000 m near the western boundary (from western coast to 38°W), interior of the section (from 39°W to 3°E), and near the eastern boundary (from 3°E to eastern coast). The AMOC geostrophic transport has a higher correlation with the western ($r = 0.69$) than with the eastern boundary ($r = 0.32$) (Figure 11). This is different to what was observed at 34.5°S, where the eastern boundary contributes more to the AMOC variability than the western boundary (Meinen et al., 2018). A possible explanation for this difference is the increased influence of the Agulhas leakage in the eastern boundary close to 34.5°S. In addition, the interior and eastern boundary transports show a significant inverse relationship ($r = -0.50$) and compensation between the two regions (blue and red curves in Figure 11). The anomalous strengthening of the AMOC in 2015 (green curve in Figure 11), where the geostrophic contribution reached values close to 31 Sv, is due to a concurrent intensification of equatorward circulation on both boundaries (black and red curves in Figure 11). Apart from that, most of the AMOC anomalous intensification events are caused by the changes in only one of the boundaries.

4. Conclusions

We use a combination of Argo and XBT data to produce the first estimate of the AMOC and MHT at 22.5°S. The current in situ coverage composed by Argo and XBT data is sufficient for the calculation of AMOC and MHT at 22.5°S from 2007 onwards. The altimetry optimized mapping method proved to be efficient in capturing westward wave propagation, coastal sea level, boundary currents, AMOC and MHT. In addition, a comparison between altimetry, AXMOC and RG Argo products suggest a multi-year SLA pattern characterized by positive anomalies from January/2007 to June/2010 and from May/2015 to December/2020, and negative between July/2010 and April/2015 (Figure 3). As this variability pattern is characteristic of the entire basin, it could be linked to large-scale climate modes.

This method allows the first continuous long-term monthly transport estimate of the BC, which was possible due to the coverage by the high-density XBT transect, which was first implemented in 2004. The estimated variability of the BC transport is comparable to its mean value, which agrees with previous studies (Lima et al., 2016). The mean and variability of the BC was 2–3 times higher than the ones estimated for RG Argo and ECCOv4r4. BC volume transport anomalies observed in 2009/2010 are consistent with Goes, Cirano, et al. (2019). These and other BC anomalies (e.g., 2014 and 2016) are captured by AXMOC data and observed in the SLA time series at the western boundary (Figures 4a and 4c black and red curves). A better match could be accomplished by comparing our product with other reanalyzes with higher spatial resolution (e.g., GLORYS, HYCOM).

Some physical properties (T, S, and γ) of the main water masses in the South Atlantic were also analyzed here, and are consistent with earlier studies (Hernández-Guerra et al., 2019; Liu & Tanhua, 2021; Stramma et al., 2004; Talley, 2011). At 22.5°S, both AABW and NADW are constrained to the west of 30°W by local topography, and the latter is divided into two cores flowing along the western and eastern boundaries near depths of 2,500 m. In the uppermost isopycnal layer ($\gamma < 27.23$ kg m^{-3}), an important area for AMOC variability, AXMOC and A9.5 data have a good agreement. The AXMOC data yields volume transports of 18.7 and 19.6 Sv for April/2009 and March/2018, respectively, while A9.5 data yields volume transports of 20.3 and 17.9 Sv for the same period, respectively. The integrated isopycnal transport obtained by AXMOC is robust and an uncertainty of ∼2 Sv in the AMOC transport due to the mapping errors is estimated from independent observations.

Seasonality in the AMOC and MHT time series shows a good agreement between all the products considered, with annual amplitudes of 4 Sv and 0.3 PW, respectively. Stronger AMOC/MHT values are observed in Jan-Jul and weaker values are observed in August-December. The geostrophic and Ekman contributions are in-phase and reinforce this variability. The interannual variability in the geostrophic component of the AMOC from AXMOC is more intense than those from other products, probably because of the improved resolution near the western boundary. The western boundary currents appear to have the largest contribution to the AMOC/MHT variability ($r = 0.62$). Our results show sharp declines in the AMOC and MHT during positive BC anomalies (intense southward transport), such as in 2014, end of 2015 and 2019. Also, a period of more frequent negative values of total and geostrophic transports in both AMOC and MHT is observed between 2010 and 2015. Further analysis is needed, but the basin wide extent of this event suggests that they are related to large scale modes of variability in the South Atlantic. Finally, AXMOC data could also be used to assess freshwater flux anomalies in the South Atlantic and to link them to a possible bi-stability of the AMOC (Rahmstorf, 1996; Stommel, 1961).

The observed AMOC (MHT) mean transport was 16.3 ± 3.2 Sv (0.7 ± 0.2 PW) between 2007 and 2020, and positive anomalies became more frequent after 2015 (Figure 10 and Figure S5 in Supporting Information S1), although this trend was not statistically significant given the uncertainty of our estimates. The AMOC is projected to weaken according to the IPCC projections for the 21st century (Collins et al., 2019; Fox-Kemper et al., 2021; Lee et al., 2021). Predictions of future AMOC weakening have been linked to a BC intensification (Marcello et al., 2023), and our results corroborate the link between the BC and the AMOC at 22.5°S, thus the continuation of this monitoring effort at 22.5°S might provide early evidence of changes in the AMOC in the Northern Hemisphere.

The availability of multi-decadal tide gauges data on both sides of the basin can be used in the future to complement, validate, and extend the DH field on the boundaries. Deep Argo profilers and/or PIES stations have the potential to improve data availability in the South Atlantic deep ocean (>2,000 m), and could replace climatological data in the deep ocean, as their spatial and temporal coverage has been increasing significantly. The proposed method can be replicated to include other latitudes in the Atlantic basin where the Argo and XBT coverage would permit a long term AMOC and MHT estimates. This expansion to other latitudes would be beneficial for the scientific community once an integrated assessment of the long-term variability of AMOC and MHT can be performed using a single method. Currently, the AMOC has been monitored at different latitudes, however, each program has different limitations and uncertainties, which impacts the comparison and integration of different time series (Chidichimo et al., 2023). In addition, our method allows more frequent updates of the AMOC than mooring arrays because Argo and XBT data are publicly available in near-real time. Therefore, our method, if expanded in time and space, could positively impact the prediction capability of different events (e.g., coastal sea level and hurricane season outlook).

Data Availability Statement

Software—All calculations and figures were performed by Matlab v.2019 (The MathWorks Inc, 2019). Data—XBT transect data (http://www.aoml.noaa.gov/phod/hdenxbt/—XBT Network, 2021); Argo profile data (https://www.nodc.noaa.gov/argo/ and https://www.seanoe.org/data/00311/42182/—Argo, 2020; http://doi.org/10.17882/42182); Argo/altimetry climatological ADT product (http://apdrc.soest.hawaii.edu/projects/argo/—IPRC, 2021); the delayed-time satellite altimetry maps (http://marine.copernicus.eu—Pujol et al., 2021); ERA5 atmospheric reanalysis (https://cds.climate.copernicus.eu—Hersbach et al., 2020); MOC and MHT synthetic time series (https://www.aoml.noaa.gov/phod/samoc_argo_altimetry/data_moc.php—Dong et al., 2015); WOA18 (https://www.ncei.noaa.gov/access/world-ocean-atlas-2018/—Locarnini et al., 2018; Zweng et al., 2019); RG

Argo (https://sio-argo.ucsd.edu/RG_Climatology.html—Roemmich & Gilson, 2009); ECCOv4r4 (https://www.ecco-group.org/products-ECCO-V4r4.htm—ECCO Consortium et al., 2022); GO-SHIP/CLIVAR (https://cchdo.ucsd.edu—King, 2022) for cruises A9.5 in 2009 (https://cchdo.ucsd.edu/cruise/740H20090307) and in 2018 (https://cchdo.ucsd.edu/cruise/740H20180228).

Acknowledgments
This research was carried out in part under the auspices of the Cooperative Institute for Marine and Atmospheric Studies, a cooperative institute of the University of Miami and the National Oceanic and Atmospheric Administration (NOAA), cooperative agreement NA20OAR4320472, and was supported by NOAA's Atlantic Oceanographic and Meteorological Laboratory (AOML). MG and DLV were also supported by the National Oceanic and Atmospheric Administration (NOAA) Climate Variability and Predictability program (Grant NA20OAR4310407).

References

Ablain, M., Meyssignac, B., Zawadzki, L., Jugier, R., Ribes, A., Spada, G., et al. (2019). Uncertainty in satellite estimates of global mean sea-level changes, trend and acceleration. *Earth System Science Data*, *11*(3), 1189–1202. https://doi.org/10.5194/essd-11-1189-2019

Argo. (2020). Argo float data and metadata from global data assembly centre (Argo GDAC) [Dataset]. SEANOE. https://doi.org/10.17882/42182

Arnault, S., Gourdeau, L., & Menard, Y. (1992). Comparison of the altimetric signal with in situ measurements in the tropical Atlantic Ocean. Deep Sea Research Part A. *Oceanographic Research Papers*, *39*(3–4), 481–499. https://doi.org/10.1016/0198-0149(92)90084-7

Arumí-Planas, C., Pérez-Hernández, M. D., Pelegrí, J. L., Vélez-Belchí, P., Emelianov, M., Caínzos, V., et al. (2023). The South Atlantic circulation between 34.5°S, 24°S and above the mid-Atlantic ridge from an inverse box model. *Journal of Geophysical Research: Oceans*, *128*(5), e2022JC019614. https://doi.org/10.1029/2022JC019614

Barron, C. N., Kara, A. B., & Jacobs, G. A. (2009). Objective estimates of westward Rossby wave and eddy propagation from sea surface height analyses. *Journal of Geophysical Research*, *114*(C3), 496–510. https://doi.org/10.1029/2008JC005044

Bellomo, K., Angeloni, M., Corti, S., & von Hardenberg, J. (2021). Future climate change shaped by inter-model differences in Atlantic meridional overturning circulation response. *Nature Communications*, *12*(1), 1–10. https://doi.org/10.1038/s41467-021-24015-w

Berger, W. H., Wefer, G., Richter, C., Lange, C. B., Giraudeau, J., Hermelin, O., & Party, S. S. (1998). 17. The Angola-Benguela upwelling system: Paleoceanographic synthesis of shipboard results from leg 1751. In *Proceedings Ocean Drilling program, initial reports* (Vol. 175, pp. 505–531). https://doi.org/10.2973/odp.proc.ir.175.117.1998

Biastoch, A., Böning, C. W., Schwarzkopf, F. U., & Lutjeharms, J. R. E. (2009). Increase in Agulhas leakage due to poleward shift of Southern Hemisphere westerlies. *Nature*, *462*(7272), 495–498. https://doi.org/10.1038/nature08519

Broecker, W. S. (2003). Does the trigger for abrupt climate change reside in the ocean or in the atmosphere? *Science*, *300*(5625), 1519–1522. https://doi.org/10.1126/science.1083797

Bryden, H. L., King, B. A., & McCarthy, G. D. (2011). South Atlantic overturning circulation at 24 S. *Journal of Marine Research*, *69*(1), 38–55. https://doi.org/10.1357/002224011798147633

Buckley, M. W., & Marshall, J. (2016). Observations, inferences, and mechanisms of the Atlantic meridional overturning circulation: A review. *Reviews of Geophysics*, *54*(1), 5–63. https://doi.org/10.1002/2015RG000493

Caínzos, V., Hernández-Guerra, A., McCarthy, G. D., McDonagh, E. L., Cubas Armas, M., & Pérez-Hernández, M. D. (2022). Thirty years of GOSHIP and WOCE data: Atlantic overturning of mass, heat, and freshwater transport. *Geophysical Research Letters*, *49*(4), e2021GL096527. https://doi.org/10.1029/2021GL096527

Calado, L., Gangopadhyay, A., & Da Silveira, I. C. A. (2008). Feature-oriented regional modeling and simulations (FORMS) for the western South Atlantic: Southeastern Brazil region. *Ocean Modelling*, *25*(1–2), 48–64. https://doi.org/10.1016/j.ocemod.2008.06.007

Chang, P., Zhang, R., Hazeleger, W., Wen, C., Wan, X., Ji, L., et al. (2008). Oceanic link between abrupt changes in the North Atlantic Ocean and the African monsoon. *Nature Geoscience*, *1*(7), 444–448. https://doi.org/10.1038/ngeo218

Chidichimo, M. P., Perez, R. C., Speich, S., Kersalé, M., Sprintall, J., Dong, S., et al. (2023). Energetic overturning flows, dynamic interocean exchanges, and ocean warming observed in the South Atlantic. *Communications Earth Environment*, *4*(1), 10. https://doi.org/10.1038/s43247-022-00644-x

Collins, M., Sutherland, M., Bouwer, L., Cheong, S. M., Frölicher, T., Jacot Des Combes, H., et al. (2019). Extremes, abrupt changes and managing risk. In H. O. Pörtner, D. C. Roberts, V. Masson-Delmotte, P. Zhai, M. Tignor, E. Poloczanska, et al. (Eds.), *IPCC special report on the Ocean and cryosphere in a changing climate* (pp. 589–655). Cambridge University Press. https://doi.org/10.1017/9781009157964.008

Conway, T. M., Palter, J. B., & de Souza, G. F. (2018). Gulf Stream rings as a source of iron to the North Atlantic subtropical gyre. *Nature Geoscience*, *11*(8), 594–598. https://doi.org/10.1038/s41561-018-0162-0

Da Silveira, I. C. A., Lima, J. A. M., Schmidt, A. C. K., Ceccopieri, W., Sartori, A., Francisco, C. P. F., & Fontes, R. F. C. (2008). Is the meander growth in the Brazil Current system off Southeast Brazil due to baroclinic instability? *Dynamics of Atmospheres and Oceans*, *45*(3–4), 187–207. https://doi.org/10.1016/j.dynatmoce.2008.01.002

Desbruyères, D., Chafik, L., & Maze, G. (2021). A shift in the ocean circulation has warmed the subpolar North Atlantic Ocean since 2016. *Commun Earth Environ*, *2*(1), 48. https://doi.org/10.1038/s43247-021-00120-y

de Vries, P., & Weber, S. L. (2005). The Atlantic freshwater budget as a diagnostic for the existence of a stable shut down of the meridional overturning circulation. *Geophysical Research Letters*, *32*(9), L09606. https://doi.org/10.1029/2004GL021450

Dong, S., Garzoli, S., Baringer, M., Meinen, C., & Goni, G. (2009). Interannual variations in the Atlantic meridional overturning circulation and its relationship with the net northward heat transport in the South Atlantic. *Geophysical Research Letters*, *36*(20), L20606. https://doi.org/10.1029/2009GL039356

Dong, S., Goni, G., & Bringas, F. (2015). Temporal variability of the South Atlantic meridional overturning circulation between 20 S and 35 S [Dataset]. Geophysical Research Letters, *42*(18), 7655–7662. https://doi.org/10.1002/2015GL065603

Dong, S., Goni, G., Domingues, R., Bringas, F., Goes, M., Christophersen, J., & Baringer, M. (2021). Synergy of in situ and satellite ocean observations in determining meridional heat transport in the Atlantic Ocean. *Journal of Geophysical Research: Oceans*, *126*(4), e2021JC017946. https://doi.org/10.1029/2020JC017073

Durgadoo, J. V., Loveday, B. R., Reason, C. J., Penven, P., & Biastoch, A. (2013). Agulhas leakage predominantly responds to the Southern Hemisphere westerlies. *Journal of Physical Oceanography*, *43*(10), 2113–2131. https://doi.org/10.1175/JPO-D-13-047.1

ECCO Consortium, Fukumori, I., Wang, O., Fenty, I., Forget, G., Heimbach, P., & Ponte, R. M. (2022). ECCO central estimate (version 4 release 4) [Dataset]. ECCO. Retrieved from https://www.ecco-group.org/products-ECCO-V4r4.htm

Forget, G., Campin, J.-M., Heimbach, P., Hill, C. N., Ponte, R. M., & Wunsch, C. (2015). ECCO version 4: An integrated framework for non-linear inverse modeling and global ocean state estimation. *Geoscientific Model Development*, *8*(10), 3071–3104. https://doi.org/10.5194/gmd-8-3071-2015

Fox-Kemper, B., Hewitt, H. T., Xiao, C., Aðalgeirsdóttir, G., Drijfhout, S. S., Edwards, T. L., et al. (2021). Ocean, cryosphere and sea level change. In V. Masson-Delmotte, P. Zhai, A. Pirani, S. L. Connors, C. Péan, S. Berger, et al. (Eds.), *Climate change 2021: The physical science*

basis. Contribution of working group I to the sixth assessment report of the intergovernmental panel on climate change (pp. 1211–1362). Cambridge University Press. https://doi.org/10.1017/9781009157896.011

Frajka-Williams, E., Ansorge, I. J., Baehr, J., Bryden, H. L., Chidichimo, M. P., Cunningham, S. A., et al. (2019). Atlantic meridional overturning circulation: Observed transport and variability. *Frontiers in Marine Science*, *6*, 260. https://doi.org/10.3389/fmars.2019.00260

Garcia, H. E., Boyer, T. P., Baranova, O. K., Locarnini, R. A., Mishonov, A. V., Grodsky, A., et al. (2019). World Ocean atlas 2018: Product documentation. In A. Mishonov (Ed.), *NOAA Atlas NESDIS*. Retrieved from https://www.ncei.noaa.gov/sites/default/files/2020-04/woa18documentation.pdf

Garzoli, S. L., Baringer, M., Dong, S., Perez, R., & Yao, Q. (2013). South Atlantic meridional fluxes. *Deep-Sea Research, Part A: Oceanographic Research Papers I*, *71*, 21–32. https://doi.org/10.1016/j.dsr.2012.09.003

Garzoli, S. L., Dong, S., Fine, R., Meinen, C. S., Perez, R. C., Schmid, C., et al. (2015). The fate of the deep western boundary current in the South Atlantic. *Deep Sea Research Part I: Oceanographic Research Papers*, *103*, 125–136. https://doi.org/10.1016/j.dsr.2015.05.008

Garzoli, S. L., & Gordon, A. L. (1996). Origins and variability of the Benguela current. *Journal of Geophysical Research*, *101*(C1), 897–906. https://doi.org/10.1029/95JC03221

Goes, M., Christophersen, J., Dong, S., Goni, G., & Baringer, M. O. (2018). An updated estimate of salinity for the Atlantic ocean sector using temperature–salinity relationships. *Journal of Atmospheric and Oceanic Technology*, *35*(9), 1771–1784. https://doi.org/10.1175/JTECH-D-18-0029.1

Goes, M., Cirano, M., Mata, M. M., & Majumder, S. (2019). Long-term monitoring of the Brazil current transport at 22°S from XBT and altimetry data: Seasonal, interannual, and extreme variability. *Journal of Geophysical Research: Oceans*, *124*(6), 3645–3663. https://doi.org/10.1029/2018JC014809

Goes, M., Goni, G., & Dong, S. (2015). An optimal XBT-based monitoring system for the South Atlantic meridional overturning circulation at 34°S. *Journal of Geophysical Research: Oceans*, *120*(1), 161–181. https://doi.org/10.1002/2014JC010202

Goes, M., Goni, G., Dong, S., Boyer, T., & Baringer, M. (2020). The complementary value of XBT and Argo observations to monitor ocean boundary currents and meridional heat and volume transports: A case study in the Atlantic Ocean. *Journal of Atmospheric and Oceanic Technology*, *37*(12), 2267–2282. https://doi.org/10.1175/JTECH-D-20-0027.1

Goes, M., Murphy, L. N., & Clement, A. C. (2019). The stability of the AMOC during Heinrich events is not dependent on the AMOC strength in an Intermediate Complexity Earth System model ensemble. *Paleoceanography and Paleoclimatology*, *34*(8), 1359–1374. https://doi.org/10.1029/2019PA003580

Goes, M., Urban, N. M., Tonkonojenkov, R., Haran, M., Schmittner, A., & Keller, K. (2010). What is the skill of ocean tracers in reducing uncertainties about ocean diapycnal mixing and projections of the Atlantic Meridional Overturning Circulation? *Journal of Geophysical Research*, *115*(C12), 3213. https://doi.org/10.1029/2010JC006407

Goes, M., Wainer, I., & Signorelli, N. (2014). Investigation of the causes of historical changes in the subsurface salinity minimum of the South Atlantic. *Journal of Geophysical Research-Oceans*, *119*(9), 5654–5675. https://doi.org/10.1002/2014JC009812

Hernández-Guerra, A., Joyce, T. M., Fraile-Nuez, E., & Vélez-Belchí, P. (2010). Using Argo data to investigate the meridional overturning circulation in the North Atlantic. *Deep Sea Research Part I: Oceanographic Research Papers*, *57*(1), 29–36. https://doi.org/10.1016/j.dsr.2009.10.003

Hernández-Guerra, A., Talley, L. D., Pelegrí, J. L., Vélez-Belchí, P., Baringer, M. O., Macdonald, A. M., & McDonagh, E. L. (2019). The upper, deep, abyssal and overturning circulation in the Atlantic Ocean at 30 S in 2003 and 2011. *Progress in Oceanography*, *176*, 102136. https://doi.org/10.1016/j.pocean.2019.102136

Herrford, J., Brandt, P., Kanzow, T., Hummels, R., Araujo, M., & Durgadoo, J. V. (2021). Seasonal variability of the Atlantic Meridional Overturning Circulation at 11 S inferred from bottom pressure measurements. *Ocean Science*, *17*(1), 265–284. https://doi.org/10.5194/os-17-265-2021

Hersbach, H., Bell, B., Berrisford, P., Hirahara, S., Horanyi, H., Munoz-Sabater, J., et al. (2020). The ERA5 global reanalysis [Dataset]. Quarterly Journal of the Royal Meteorological Society, *146*(730), 1999–2049. https://doi.org/10.1002/qj.3803

Hummels, R., Brandt, P., Dengler, M., Fischer, J., Araujo, M., Veleda, D., & Durgadoo, J. V. (2015). Interannual to decadal changes in the western boundary circulation in the Atlantic at 11°S. *Geophysical Research Letters*, *42*(18), 7615–7622. https://doi.org/10.1002/2015GL065254

IPRC. (2021). Argo/altimetry climatological ADT product [Dataset]. IPRC. Retrieved from http://apdrc.soest.hawaii.edu/projects/argo/

Johns, W. E., Baringer, M. O., Beal, L. M., Cunningham, S. A., Kanzow, T., Bryden, H. L., et al. (2011). Continuous, array-based estimates of Atlantic Ocean heat transport at 26.5 N. *Journal of Climate*, *24*(10), 2429–2449. https://doi.org/10.1175/2010JCLI3997.1

Kersalé, M., Meinen, C. S., Perez, R. C., Le Henaff, M., Valla, D., Lamont, T., et al. (2020). Highly variable upper and abyssal overturning cells in the South Atlantic. *Science Advances*, *6*(32), eaba7573. https://doi.org/10.1126/sciadv.aba7573

King, B. A. (2022). CTD data from cruises 740H20090307 and 740H20180228, NetCDF [Dataset]. CCHDO. Retrieved from https://cchdo.ucsd.edu/cruise/740H20090307

Lebedev, K. V., Yoshinari, H., Maximenko, N. A., & Hacker, P. W. (2007). Velocity data assessed from trajectories of Argo floats at parking level and at sea surface. *IPRC Technical Note*, *4*(2), 1–16.

Lee, J.-Y., Marotzke, J., Bala, G., Cao, L., Corti, S., Dunne, J. P., et al. (2021). Future global climate: Scenario-based projections and near-term information. In V. Masson-Delmotte, P. Zhai, A. Pirani, S. L. Connors, C. Péan, S. Berger, et al. (Eds.), *Climate change 2021: The physical science basis. Contribution of working group I to the sixth assessment report of the intergovernmental panel on climate change* (pp. 553–672). Cambridge University Press. https://doi.org/10.1017/9781009157896.006

Lima, M. O., Cirano, M., Mata, M. M., Goes, M., Goni, G., & Baringer, M. (2016). An assessment of the Brazil current baroclinic structure and variability near 22°S in distinct ocean forecasting and analysis systems. *Ocean Dynamics*, *66*(6), 893–916. https://doi.org/10.1007/s10236-016-0959-6

Little, C. M., Piecuch, C. G., & Ponte, R. M. (2017). On the relationship between the meridional overturning circulation, alongshore wind stress, and United States East Coast sea level in the Community Earth System Model Large Ensemble. *Journal of Geophysical Research*, *112*(6), 4554–4568. https://doi.org/10.1002/2017JC012713

Liu, M., & Tanhua, T. (2021). Water masses in the Atlantic Ocean: Characteristics and distributions. *Ocean Science*, *17*(2), 463–486. https://doi.org/10.5194/os-17-463-2021

Locarnini, M. M., Mishonov, A. V., Baranova, O. K., Boyer, T. P., Zweng, M. M., Garcia, H. E., et al. (2018). World ocean atlas 2018, volume 1: Temperature [Dataset]. In A. Mishonov (Ed.) *NOAA Atlas NESDIS 81* (p. 52). Retrieved from https://www.ncei.noaa.gov/sites/default/files/2020-04/woa18_vol1.pdf

Lopez, H., Dong, S., Lee, S.-K., & Goni, G. (2016). Decadal modulations of interhemispheric global atmospheric circulations and Monsoons by the South Atlantic meridional overturning circulation. *Journal of Climate*, *29*(5), 1831–1851. https://doi.org/10.1175/JCLI-D-15-0491.1

Lux, M., Mercier, H., & Arhan, M. (2001). Interhemispheric exchanges of mass and heat in the Atlantic Ocean in January–March 1993. *Deep Sea Research Part I: Oceanographic Research Papers*, *48*(3), 605–638. https://doi.org/10.1016/S0967-0637(00)00033-9

Majumder, S., & Schmid, C. (2018). A study of the variability in the Benguela Current volume transport. *Ocean Science*, *14*(2), 273–283. https://doi.org/10.5194/os-14-273-2018

Majumder, S., Schmid, C., & Halliwell, G. (2016). An observations and model-based analysis of meridional transports in the South Atlantic. *Journal of Geophysical Research: Oceans*, *121*(8), 5622–5638. https://doi.org/10.1002/2016JC011693

Marcello, F., Tonelli, M., Ferrero, B., & Wainer, I. (2023). Projected Atlantic overturning slow-down is to be compensated by a strengthened South Atlantic subtropical gyre. *Commun Earth Environ*, *4*(1), 92. https://doi.org/10.1038/s43247-023-00750-4

Mata, M. M., Cirano, M., Caspel, M. R. V., Fonteles, C. S., Gõni, G., & Baringer, M. (2012). Observations of Brazil Current baroclinic transport near 22 S: Variability from the AX97 XBT transect. *Exchanges*, *58*, 5–10.

McCarthy, G. D., Brown, P. J., Flagg, C. N., Goni, G., Houpert, L., Hughes, C. W., et al. (2020). Sustainable observations of the AMOC: Methodology and technology. *Reviews of Geophysics*, *58*(1), e2019RG000654. https://doi.org/10.1029/2019RG000654

Meinen, C. S., Speich, S., Piola, A. R., Ansorge, I., Campos, E., Kersalé, M., et al. (2018). Meridional overturning circulation transport variability at 34.5 S during 2009–2017: Baroclinic and barotropic flows and the dueling influence of the boundaries. *Geophysical Research Letters*, *45*(9), 4180–4188. https://doi.org/10.1029/2018GL077408

Pereira, J., Gabioux, M., Almeida, M. M., Cirano, M., Paiva, A. M., & Aguiar, A. L. (2014). The bifurcation of the western boundary current system of the South Atlantic Ocean. *Brazilian Journal of Genetics*, *32*(2), 241–257. https://doi.org/10.22564/rbgf.v32i2.456

Pita, I. I., Cirano, M., & Mata, M. M. (2020). An assessment of Brazil current surface velocity and associated transport near 22° S: XBT and altimetry data. *Regional Studies in Marine Science*, *35*, 101197. https://doi.org/10.1016/j.rsma.2020.101197

Polito, P. S., & Liu, W. T. (2003). Global characterization of Rossby waves at several spectral bands. *Journal of Geophysical Research*, *108*(C1), 97. https://doi.org/10.1029/2000JC000607

Pujol, M. I., Faugère, Y., Taburet, G., Dupuy, S., Pelloquin, C., Ablain, M., & Picot, N. (2016). DUACS DT2014: The new multi-mission altimeter data set reprocessed over 20 years. *Ocean Science*, *12*(5), 1067–1090. https://doi.org/10.5194/os-12-1067-2016

Pujol, M.-I., Taburet, G., & SL-TAC team. (2021). Sea level TAC—DUACS products [Dataset]. Copernicus Marine. https://doi.org/10.48670/moi-00148

Rahmstorf, S. (1996). On the freshwater forcing and transport of the Atlantic thermohaline circulation. *Climate Dynamics*, *12*(12), 799–811. https://doi.org/10.1007/s003820050144

Reid, J. L. (1989). On the total geostrophic circulation of the South Atlantic Ocean: Flow patterns, tracers, and transports. *Progress in Oceanography*, *23*(3), 149–244. https://doi.org/10.1016/0079-6611(89)90001-3

Rhein, M. (2019). Taking a close look at ocean circulation. *Science*, *363*(6426), 456–457. https://doi.org/10.1126/science.aaw3111

Rio, M. H., Guinehut, S., & Larnicol, G. (2011). New CNES-CLS09 global mean dynamic topography computed from the combination of GRACE data, altimetry, and in situ measurements. *Journal of Geophysical Research*, *116*(C7), 1–25. https://doi.org/10.1029/2010JC006505

Roemmich, D., & Gilson, J. (2009). The 2004–2008 mean and annual cycle of temperature, salinity, and steric height in the global ocean from the Argo Program [Dataset]. Progress in Oceanography, *82*(2), 81–100. https://doi.org/10.1016/j.pocean.2009.03.004

Roemmich, D., Johnson, G. C., Riser, S., Davis, R., Gilson, J., Owens, W. B., et al. (2009). The Argo Program: Observing the global ocean with profiling floats. *Oceanography*, *22*(2), 34–43. https://doi.org/10.5670/oceanog.2009.36

Stommel, H. (1961). Thermohaline convection with two stable regimes of flow. *Tellus*, *13*(2), 224–230. https://doi.org/10.1111/j.2153-3490.1961.tb00079.x

Stramma, L., Kieke, D., Rhein, M., Schott, F., Yashayaev, I., & Koltermann, K. P. (2004). Deep water changes at the western boundary of the subpolar North Atlantic during 1996 to 2001. *Deep-Sea Research*, *51*(8), 1033–1056. https://doi.org/10.1016/j.dsr.2004.04.001

Strub, P. T., James, C., Combes, V., Matano, R. P., Piola, A. R., Palma, E. D., et al. (2015). Altimeter-derived seasonal circulation on the southwest Atlantic shelf: 27°–43°S. *Journal of Geophysical Research: Oceans*, *120*(5), 3391–3418. https://doi.org/10.1002/2015JC010769

Talley, L. D. (2011). *Descriptive physical oceanography: An introduction* (6th ed., p. 560). Academic Press.

Talley, L. D., Feely, R. A., Sloyan, B. M., Wanninkhof, R., Baringer, M. O., Bullister, J. L., et al. (2016). Changes in ocean heat, carbon content, and ventilation: A review of the first decade of GO-SHIP global repeat hydrography. *Annual Review of Marine Science*, *8*(1), 185–215. https://doi.org/10.1146/annurev-marine-052915-100829

The MathWorks Inc. (2019). MATLAB version: 9.6.0.1135713 update 3 (R2019a), 722 Natick, Massachusetts [Software]. The MathWorks Inc. Retrieved from https://www.mathworks.com

Todd, R. E., Chavez, F. P., Clayton, S., Cravatte, S., Goes, M., Graco, M., et al. (2019). Global perspectives on observing ocean boundary current systems. *Frontiers in Marine Science*, *6*(423), 25. https://doi.org/10.3389/fmars.2019.00423

Volkov, D. L., Baringer, M., Smeed, D., Johns, W., & Landerer, F. W. (2019). Teleconnection between the Atlantic meridional overturning circulation and sea level in the Mediterranean Sea. *Journal of Climate*, *32*(3), 935–955. https://doi.org/10.1175/JCLI-D-18-0474.1

Volkov, D. L., Lee, S.-K., Domingues, R., Zhang, H., & Goes, M. (2019). Interannual sea level variability along the southeastern seaboard of the United States in relation to the gyre-scale heat divergence in the North Atlantic. *Geophysical Research Letters*, *46*(13), 7481–7490. https://doi.org/10.1029/2019GL083596

Volkov, D. L., Smeed, D. A., Lankhorst, M., Dong, S., Moat, I., Willis, J., et al. (2023). Meridional overturning circulation and heat transport in the Atlantic Ocean. In J. Blunden, T. Boyer, & E. Bartow-Gillies (Eds.), *2023: "State of the climate in 2022". Bulletin of the American Meteorological Society 9* (Vol. 104, p. Si-S501). https://doi.org/10.1175/2023BAMSStateoftheClimate.1

Volkov, D. L., Zhang, K., Johns, W., Willis, J., Hobbs, W., Goes, M., et al. (2023). Atlantic meridional overturning circulation increases flood risk along the United States southeast coast. *Nature Communications*, *14*(1), 5095. https://doi.org/10.1038/s41467-023-40848-z

Weijer, W., Cheng, W., Drijfhout, S. S., Fedorov, A. V., Hu, A., Jackson, L. C., et al. (2019). Stability of the Atlantic meridional overturning circulation: A review and synthesis. *Journal of Geophysical Research: Oceans*, *124*(8), 5336–5375. https://doi.org/10.1029/2019JC015083

XBT Network. (2021). High density XBT transect data from physical Oceanography Division (PhOD), Atlantic Oceanographic and Meteorological Laboratory (AOML) [Dataset]. National Oceanic and Atmospheric Administration. Retrieved from http://www.aoml.noaa.gov/phod/hdenxbt/

Zweng, M. M., Seidov, D., Boyer, T. P., Locarnini, M., Garcia, H. E., Mishonov, A. V., et al. (2019). World ocean atlas 2018, volume 2: Salinity [Dataset]. In A. Mishonov (Ed.) *NOAA Atlas NESDIS 82* (p. 50). Retrieved from https://www.ncei.noaa.gov/sites/default/files/2022-06/woa18_vol2.pdf